

Trans-Neptunian objects and Centaurs at thermal wavelengths

Thomas Müller¹[0000-0002-0717-0462], Emmanuel Lellouch²[0000-0001-7168-1577], and
Sonia Fornasier²[0000-0001-7678-3310]

¹ Max-Planck-Institut für extraterrestrische Physik, Giessenbachstrasse 1, 85748 Garching, Germany; tmueller@mpe.mpg.de

² LESIA, Observatoire de Paris, Université PSL, CNRS, Univ. Paris Diderot, Sorbonne Paris Cité, Sorbonne Université, 5 Place J. Janssen, 92195 Meudon Pricipal Cedex, France

Abstract. The thermal emission of transneptunian objects (TNO) and Centaurs has been observed at mid- and far-infrared wavelengths - with the biggest contributions coming from the Spitzer and Herschel space observatories-, and the brightest ones also at sub-millimeter and millimeter wavelengths. These measurements allowed to determine the sizes and albedos for almost 180 objects, and densities for about 25 multiple systems. The derived very low thermal inertias show evidence for a decrease at large heliocentric distances and for high-albedo objects, which indicates porous and low-conductivity surfaces. The radio emissivity was found to be low ($\epsilon_r=0.70\pm 0.13$) with possible spectral variations in a few cases. The general increase of density with object size points to different formation locations or times. The mean albedos increase from about 5-6% (Centaurs, Scattered-Disk Objects) to 15% for the Detached objects, with distinct cumulative albedo distributions for hot and cold classicals. The color-albedo separation in our sample is evidence for a compositional discontinuity in the young Solar System. The median albedo of the sample (excluding dwarf planets and the Haumea family) is 0.08, the albedo of Haumea family members is close to 0.5, best explained by the presence of water ice. The existing thermal measurements remain a treasure trove at times where the far-infrared regime is observationally not accessible.

Keywords: Infrared observations · Kuiper belt · Photometry · Trans-neptunian objects.

1 Introduction

Thermal IR observations are crucial for the physical and thermal characterization of distant objects which are typically too small to be resolved even by the largest ground or space telescopes. The thermal emission measurements allow one to determine accurate radiometric size and albedo information, but they also put constraints on the object's thermal properties and spin-axis orientations. Albedos derived from thermal data are important to interpret broad-band colors and NIR spectral data. The submm/mm-range emission originates from a few millimeters below the surface and can be used to determine the object's long-wavelength emissivity. A recent new approach is to combine multi-data information (occultations, thermal, high-resolution imaging, etc.) to perform

more sophisticated physical and thermal characterization of TNOs and Centaurs, and to constrain properties which are otherwise not accessible, for example the object's spin-axis orientation. At the same time, the multi-disciplinary approach allows to improve and extend model techniques, e.g., the verification of radiometric sizes via occultation results. A comparison between radiometric and occultation size values is given in Ortiz et al. (same book).

However, the thermal emission from TNOs and Centaurs³ is difficult to detect, mainly due to their large distance from the Sun (and the observer) and their low surface temperatures⁴.

We give an overview of the existing thermal emission measurements for TNOs and Centaurs (Section 2), the modeling concepts (Section 3), and we present the derived radiometric properties (Sections 4 and 5). The chapter is concluded by a short outlook (Section 6).

2 Thermal data for TNOs and Centaurs

The thermal infrared (IR) covers approximately the wavelength range from about 5 to 300 μm , often sub-divided into the mid-IR (MIR) range up to about 30 μm (ground-based N-/Q-band, SOFIA⁵, WISE/NEOWISE⁶, AKARI⁷, Spitzer⁸-IRS/IRAC) and the far-IR (FIR) at wavelengths up to several hundred micron (Herschel⁹-PACS, Spitzer-MIPS), followed by the sub-millimeter (submm) range below 1 mm wavelength (e.g., Herschel-SPIRE; CSO¹⁰; ALMA¹¹ bands 7-10), and the millimeter (mm) range (e.g., IRAM¹², ALMA bands 1-6, NOEMA¹³).

The first thermal measurements for a Centaur go back to ground-based infrared and IRAS measurements of Chiron (Lebofsky et al. 1984; Sykes & Walker 1991; Campins et al. 1994), followed by millimeter observations (Jewitt & Luu 1992; Altenhoff & Stumpff 1995). Pholus (Howell et al. 1992; Davies et al. 1993) and Chariklo (Jewitt & Kalas 1998) were next, with solid detections mainly in Q-band at $\sim 20 \mu\text{m}$. A first overview of the physical characteristics of TNOs and Centaurs (Davies 2000) listed sizes for 8 Centaurs (3 based on thermal measurements, other sizes are estimated as-

³ We use the term "trans-Neptunian object (TNO)" or "(Edgeworth-) Kuiper Belt object (KBO)" to describe objects with orbits in the range 30 to 50 AU, including also the Scattered-disk objects (SDO) with high eccentricities and inclinations. The Centaurs are closer and partly active objects with perihelia between Jupiter and Neptune.

⁴ Blackbody radiation from TNOs and Centaurs peaks in the FIR between 50 and 100 μm , a range which is only accessible from outside the Earth's atmosphere.

⁵ <https://www.sofia.usra.edu/>

⁶ <https://neowise.ipac.caltech.edu/>

⁷ <https://www.ir.isas.jaxa.jp/AKARI/>

⁸ <http://www.spitzer.caltech.edu/>

⁹ <http://sci.esa.int/herschel/>

¹⁰ <http://www.cso.caltech.edu/>

¹¹ <http://www.almaobservatory.org/>

¹² <http://www.iram-institute.org/>

¹³ <http://iram-institute.org/EN/noema-project.php>

suming an albedo of 4%) and no TNO sizes (Pluto was still considered as planet at that time).

The Pluto-Charon system had the first thermal detections by IRAS in 1983 (Aumann & Walker 1987, Sykes et al. 1987, Tedesco et al. 1987) and a decade later at submm/mm (Stern et al. 1993, Jewitt 1994). The characterisation of the system's IR and millimeter variability and the corresponding modeling followed: Sykes (1999) using re-analysed IRAS data, Lellouch et al. (2000a) interpreting dedicated ISO-ISOPHOT measurements, and Lellouch et al. (2000b) by searching for variability in Pluto's millimeter-wave emission. ISO also contributed with low-SNR FIR detections of two TNOs: 15789 (1993 SC) and 15874 (1996 TL66) (Thomas et al. 2000). In the years after, Varuna was measured in the submm (Jewitt et al. 2001) and mm (Lellouch et al. 2002), the Centaurs Asbolus and Chiron (Fernández et al. 2002) were detected at MIR, Chiron and Chariklo also at FIR/submm/mm (Altenhoff et al. 2001; Groussin et al. 2004), the TNOs 55565 (2002 AW197) (Margot et al. 2002), 47171 Lempo (1999 TC36) (Altenhoff et al. 2004) and Eris (Bertoldi et al. 2006) at radio wavelengths. However, many attempts to measure the TNO thermal emission produced only upper limits (e.g. Altenhoff et al. 2004; Brown et al. 2004; Ortiz et al. 2004). This changed dramatically with the availability of the Spitzer Space Telescope: Stansberry et al. (2004) reported Spitzer-MIPS FIR detections of 14 KBOs and 8 Centaurs, Grundy et al. (2005) covered 20 TNOs, followed by several other Spitzer-related TNO or Centaur projects (Cruikshank et al. 2005, 2006; Stansberry et al. 2006; Grundy et al. 2007,2008). Stansberry et al. (2008) summarized the Spitzer-provided constraints on the physical properties of 47 KBOs and Centaurs. In the years after, the Spitzer-based studies focused either on individual TNOs or smaller samples (e.g. Brucker et al. 2009; Stansberry et al. 2012). Four Centaurs and seven TNOs were also detected with AKARI (T. Sekiguchi, priv. comm.), however, no fluxes or radiometric results were published so far.

The next big step in thermal observations of Centaurs and TNOs came with Herschel's large Open Time Key Project on "TNOs are Cool: A survey of the trans-Neptunian region with Herschel" (Müller et al. 2009) which produced more than 20 publications. The Herschel data (partly also Spitzer data) allowed to interpret the thermal emission of almost 170 TNOs and Centaurs: Müller et al. 2010; Lellouch et al. 2010; Lim et al. 2010; Barucci et al. 2012; Mommert et al. 2012; Pál et al. 2012; Santos-Sanz et al. 2012; Vilenius et al. 2012; Fornasier et al. 2013; Kiss et al. 2013; Lellouch et al. 2013; Duffard et al. 2014; Lacerda et al. 2014; Vilenius et al. 2014; Marton et al. 2015; Pál et al. 2015; Kiss et al. 2016; Lellouch et al. 2016; Pál et al. 2016; Kovalenko et al. 2017; Santos-Sanz et al. 2017; Kiss et al. 2018; Müller et al. 2018; Vilenius et al. 2018.

In parallel, the WISE project performed an all-sky survey at MIR wavelengths and detected the brightest Centaurs (Bauer et al. 2013).

Since Spitzer and Herschel, the situation has become much more difficult and only a dozen TNOs have been observed in the submm/mm range, mainly by ALMA (Moulet et al. 2011; Gerdes et al. 2017; Brown & Butler 2017, 2018; Lellouch et al. 2017).

3 Radiometric techniques

3.1 Models to interpret thermal measurements

Radiometry is a powerful technique to derive size, albedo, and thermal properties from thermal infrared measurements. The technique consists in the exploitation and interpretation of thermal data (see Section 2) in combination with data in the visible. The visible data are mainly obtained from the ground and include the object’s absolute magnitude and estimates for the phase integral q . The most accurate radiometric properties are determined when objects are observed close to their thermal emission peaks, preferentially shortwards and longwards of the peak. For Centaurs and TNOs these peaks are located in the FIR regime between ≈ 50 and $100 \mu\text{m}$ (accessible from space only).

There are different thermal models to obtain size and albedo of atmosphereless small bodies: simple models like the Standard Thermal Model (STM), the Fast Rotating Thermal Model (FRM), or the near-Earth asteroid thermal model (NEATM) or more complex thermophysical models (TPM) are used (see Delbo’ et al. 2015 for a detailed discussion). For Centaurs and TNOs, mostly the NEATM (Harris 1998) and the TPM (Lagerros 1996, 1997, 1998; Müller & Lagerros 1998, 2002) are applied. In cases where the object is lacking shape or spin properties, the NEATM is often used. The beaming factor η is then either fitted to multi-band thermal measurements or a default value is applied. The STM/NEATM concepts can also handle elongated shapes (Brown 1985; Lellouch et al. 2017; Vilenius et al. 2018), but have severe limitations when thermal measurements cover different aspect angles¹⁴.

In cases where the rotation period is known, the TPM concepts have the advantage that in addition to the standard size-albedo solution, also the spin-axis and thermophysical parameters can be constrained (Fornasier et al. 2013; Kiss et al. 2018; Müller et al. 2018). Pál et al. (2012) applied STM and TPM techniques to the Herschel measurements of (90377) Sedna and 2010 EK139. The derived size-albedo values agree within $\sim 10\%$. Pál et al. (2016) also show that NEATM (fitted beaming factor) and TPM (assuming equator-on viewing geometry) approaches lead to the same size-albedo conclusions for (225088) 2007 OR10. However, the discovery of a satellite (Kiss et al. 2017) suggests a nearly pole-on viewing geometry for 2007 OR10. The recalculated TPM size (Kiss et al. 2018) is 18% smaller than the NEATM best- η solution, but agrees within 5% when assuming a default $\eta = 1.2$ in the radiometric calculations, indicating that NEATM solutions require a proper error handling for the fits of the beaming factors.

The TPM concept has advantages when objects have known spin or shape properties, or in cases where multi-epoch thermal data for different observing geometries (like for Centaurs observed over a wide range of heliocentric distances or aspect angles) are available (e.g. Kiss et al. 2013). Recently, stellar occultations by Centaurs and TNOs revealed ring systems, elongated shapes, constraints on possible atmospheres, and very accurate size information (see Ortiz et al., same volume). Here, the TPM applications allow to determine the object’s thermal properties and testing of the spin-axis orientation (Kiss et al. 2013; Müller et al. 2018). For multi-wavelength thermal data which include also submm/mm observations, a wavelength-dependent emissivity within the

¹⁴ The aspect angle is defined such that it equals 0° when we observe the North pole and it equals 180° when we observe the South pole.

TPM code is necessary to explain the observed fluxes (Fornasier et al. 2013; Lellouch et al. 2017).

The accuracy of the radiometrically derived size and albedo values depends very much on the model input values: a good-quality H-magnitude is needed for deriving the object's albedo. A typical 0.1 mag error for H translates into a $\sim 10\%$ error in geometric albedo. The thermal flux error is crucial for the final size accuracy, but here the beaming parameter (or thermal inertia and surface roughness in case of the TPM) and the object's emissivity are also relevant. In general, the final quality of the radiometric size benefits from high-quality multi-epoch and multi-wavelengths observations. It is also important to mention that radiometric solutions for high-albedo dwarf planets like Pluto, Eris, Makemake suffer from unknowns for the object's surface scattering properties, expressed in the phase integral (Stansberry et al. 2008). Using the formula $q = 0.336p_V + 0.479$, with q being the phase integral and p_V the object's geometric V-band albedo, by Brucker et al. (2009) solves only part of the problem since individual objects can deviate significantly from that relation (Verbiscer et al. 2018). To account for a wide range of scattering properties for icy surfaces, Müller et al. (2018) used a phase integral of $q = 0.65 \pm 0.20$ for Haumea which has a geometric albedo of $p_V = 0.51$ (Ortiz et al. 2017). For higher-albedo objects the uncertainty in q might be even larger, for lower-albedo objects the phase integral is less relevant and a default value of 0.39 (Bowell et al. 1989) can be used.

3.2 Satellite thermal emission

Almost all large TNOs have satellites (Parker et al. 2016b; Kiss et al. 2017) and these satellites can contribute to the observed thermal emission measurements. At MIR and FIR it was so far not possible to resolve the satellite and the main-body emission with the current technical limitations. Only in the submm/mm range it is possible to detect large satellites around dwarf planets with the high spatial resolution of the ALMA array. Brown & Butler (2018) examined the spatially resolved Orcus-Vanth and Eris-Dysnomia systems and found low albedos similar to other TNOs of similar size and different from the main body's properties. It is therefore reasonable to estimate the thermal emission of satellites by using adequate beaming and albedo properties from published statistical analysis of TNO samples. However, the thermal emission estimate for satellites remains uncertain. This has to be considered in the radiometric analysis in cases where primaries and secondaries cannot be seen directly (e.g., for 2007 OR10: see discussion in Kiss et al. 2018; for Haumea: see discussion in Müller et al. 2018).

3.3 Ring thermal emission

Rings have been detected around Chariklo (Braga-Ribas et al. 2014) and Haumea (Ortiz et al. 2017) and are suspected on other bodies (e.g. Ortiz et al. 2015). Lellouch et al. (2017) estimated the contribution of rings to thermal emission, using a simplified version of a model for Saturn's rings. In this model, the only source of energy for ring particles is absorbed solar radiation, but mutual shadowing – as seen both from the Sun and the observer – and optical depth effects are taken into consideration. The model further assumes that ring particles have a bolometric and spectral emissivity of unity.

By analogy with Saturn’s rings, the latter assumption is likely valid up to $\sim 200 \mu\text{m}$, but the spectral emissivity could decrease at longer wavelengths if ring particles are made of water ice. Model free parameters are the ring radius, width, opacity, and Bond albedo (related to the I/F reflectivity). The relative importance of ring contribution to solid body emission is of course strongly geometry-dependent, but was found to have a minor effect, e.g. affecting the equivalent diameter determination by at most 5 % for Chariklo. In that sense, for ellipsoid bodies, including/omitting rings is much less important than properly accounting for the varying pole orientation and hence projected surface of the object.

4 Albedos, sizes and densities

[HERE FIGURE 1]

Sizes, albedos, and in many cases beaming factors, derived from Spitzer, WISE and Herschel thermal data, are available for 178 TNOs and Centaurs and listed in Table 3. Transneptunian bodies show a huge diversity both in albedo and size (Fig. 1, left side). Measured diameters range from a few tens of km to ~ 2000 km but the distribution of sizes is strongly affected by discovery and selection biases in the Spitzer/Herschel/WISE sample. Eleven objects have diameters larger than 900 km: Charon, Orcus, Quaoar, Salacia, 2002 MS₄, 2007 OR₁₀, Sedna and the 4 so-called dwarf planets Pluto, Eris, Makemake and Haumea. Geometric albedos p_V vary over a factor of ~ 25 -30 from $p_V = 3 - 4\%$ for the darkest objects to $p_V \sim 50$ -90% for the brightest (see Table 3). The latter category includes 1) volatile-rich bodies (Eris, Makemake, Pluto), where the high albedo likely results from seasonally-variable resurfacing processes (deposition of fresh ice); 2) Haumea and some of its collisional family members, covered by pure H₂O ice likely excavated from Haumea’s mantle. Excluding these bodies, the vast majority of TNOs have albedos ranging from 4 to 25 %, with a median (mean & standard deviation) of 8% ($10 \pm 6\%$), see Table 1. As routinely assumed, H_V magnitude is a good proxy for size (Fig. 1, right side): using a 10 % albedo ensures an error on the diameter lower than a factor of 1.6. Fig. 1 (left side) further shows that except for the very bright objects, there is no obvious correlation between albedo and diameter, the only trend being (except for one outlier, 2005 UJ₄₃₈, whose radiometric solution may be flawed by coma activity) the lack of objects with albedos > 0.2 at diameters < 100 km. In Table 1 we present the median, mean, standard deviation σ , the error of the mean (σ/\sqrt{n}), and the minimum and maximum albedo values for each dynamic group. In the calculations we excluded the objects which have only upper/lower-limit radiometric solutions. For the Hot Classicals and the Detached categories, we present these values with and without the dwarf planets and the Haumea family. We also looked at the weighted mean albedos which are typically below the median values. But the albedo errors are closely connected to the H-magnitude errors which are coming from different sources, including rough estimates or affected by unknown opposition effects and different handling of lightcurve amplitudes. It is therefore problematic to work with error-weighted albedos.

Twenty-six binary systems with known system masses have equivalent diameter values, yielding density estimates. Density values are reported in Sicardy et al. (2011), Mommert et al. (2012), Ortiz et al. (2012, 2017), Santos-Sanz et al. (2012), Vilenius et

al. (2012, 2014), Brown (2013), Fornasier et al. (2013), Lellouch et al. (2013), Brown & Butler (2017), Dias-Oliveira et al. (2017), Kovalenko et al. (2017), Leiva et al. (2017), Kiss et al. (2018), and Stern et al. (2018). The derived bulk densities span a wide range, from below that of water ice to that of nearly pure rock (Fig. 2). TNOs smaller than 400 km have density lower than 1 g/cm^3 , as already noticed (for 1999 TC₃₆; Stansberry et al. 2006), and this implies both a small rock-to-ice ratio and a high porosity. Possible outliers are the cold classical Borasisi and the 2:1 resonant body 2002 WC₁₉; those may have higher densities but uncertainties are huge. For comparison, precise measurement of the 67P/Churyumov Gerasimenko nucleus by the Rosetta mission yields a density of $537.8 \pm 0.7 \text{ kg/m}^3$, and a large porosity (70-80%, Sierks et al. 2015; Pätzold et al. 2016; Preusker et al. 2017). Vilenius et al. (2014) also found that the sizes of the binaries components for objects smaller than 400 km are not significantly different from each other.

[HERE FIGURE 2]

The general increase of density with object size (Fig. 2) may be partly explained by gravitational self-compaction, reducing the macroporosity. However, this process alone seems unlikely to explain the factor-of-five variation of density from small to large bodies, so that large KBOs may truly be rock-richer than small ones. Thus accreting large rock-rich KBOs from smaller, rock-poor bodies is not a viable scenario (Brown 2013). Dwarf planets may have larger rock-to-ice ratios possibly due to different formation location/times compared to smaller ones. Barr & Schwamb (2016) note that among dwarf planets, those with large moons tend to have smaller densities than those with small moons¹⁵. They propose that low-velocity collisions between undifferentiated primordial dwarf planets make large planet/moon pairs, in which both bodies retain their original compositions, while higher velocity collisions between differentiated dwarf planets could yield rock-enriched primaries with small ice-rich satellites.

The median albedos increase from ~5-6% for Centaurs and Scattering Disk objects (SDO) to ~8-10% for Hot Classicals and Plutinos, to ~14% for Cold Classicals and to $\geq 15\%$ for Detached objects (see Table 1). Within the Classicals, the cold and hot populations have a clearly distinct albedo cumulative probability distributions. Given the clustering of objects in two groups in the color-albedo diagram (Lacerda et al. 2014), and the hypothesis that colors reflect the formation distance (Brown et al. 2011), this indicates that cold and hot classicals likely formed in different regions of the Solar System. Particularly remarkable is the similarity of the albedo distribution of Centaurs and SDO (median $p_V = 5-6\%$, Lacerda et al. 2014, and Table 1). It is consistent with an origin of Centaurs in the Scattered Disk (Volk & Malhotra 2008), and may suggest that these transitioning objects do not change surface properties when entering the Giant Planet region, although Jewitt (2009) and Melita & Licandro (2012) have advocated that the color bimodality of Centaurs is caused by differential thermal processing.

¹⁵ However, Fig. 2 in Barr & Schwamb (2016) suggests that the correlation between density and satellite mass ratio is not strong.

Table 1. Average albedo values for different dynamic groups: the number of objects in a given sample (n), the median albedo value, the mean and standard deviation (σ), the standard error of the mean (σ/\sqrt{n}), the minimum and maximum values (min/max) in the sample, and comments on the sample: "all" refers to all entries in Table 3 with diameter and albedo solutions, excluding the objects with only upper/lower limit solutions. In cases of dwarf planets within a given dynamic group we list the values with and without these special objects.

Dynamic group	n	median	mean	σ	σ/\sqrt{n}	min/max	comment
Cold Classical	17	0.136	0.132	0.045	0.0109	0.054	0.236 all
Hot Classical	32	0.107	0.195	0.225	0.0397	0.032	0.804 all
	26	0.084	0.102	0.072	0.0141	0.032	0.310 without Makemake, Haumea & family
Plutino	25	0.089	0.114	0.064	0.0128	0.039	0.281 without Pluto/Charon
Outer Resonant	11	0.163	0.148	0.071	0.0215	0.049	0.297 all ¹
Detached	8	0.167	0.291	0.294	0.1040	0.079	0.960 all
	7	0.148	0.195	0.125	0.0471	0.079	0.410 without Eris
SDO	20	0.057	0.075	0.046	0.0103	0.037	0.231 all
Haumea family	9		median	0.48 ^{+0.28} _{-0.18}			Vilenius et al. 2018
Centaur	55	0.056	0.074	0.043	0.0058	0.020	0.256 all
All TNOs & Centaurs	170	0.083	0.126	0.138	0.0106	0.020	0.960 all
	160	0.083	0.099	0.062	0.0049	0.020	0.328 without P/C,E,M,S,H,Hfam ²

¹ : 2001 YH140 is in a 3:5 resonance with Neptune and not considered here;

² : Pluto/Charon, Eris, Makemake, Sedna, Haumea & Haumea family members.

4.1 Classical population

Classicals - as well as the other dynamical classes - are defined according to the Gladman et al. (2008) dynamical classification. Vilenius et al. (2012, 2014) analyzed 44 classical TNOs, whose sizes range from ~ 130 to 930 km, from the Herschel and Spitzer thermal data. Classicals are distinguished between the cold and hot populations according to inclination with a limit at 5° .

Vilenius and co-workers found that the cold and hot classical populations are distinct in terms of size and albedo. First, they have different averaged albedos, as previously noticed (Grundy et al. 2005; Brucker et al. 2009): the cold classicals have a median albedo of 14% (mean: $13 \pm 5\%$ on a sample of 17 objects), higher than that of the hot population with 8% (mean $10 \pm 7\%$ from a sample of 26 objects), excluding the Haumea family members. Second, they have different (debiased) size distributions: cold classicals are smaller than 400 km, while the hot ones have a wider size distribution, and diameters up to ~ 900 km (excluding Makemake). The cumulative size distribution is also clearly different, having a much steeper slope ($q=5.1\pm 1.1$) for cold than for hot ($q=2.3\pm 0.1$) classicals, evaluated for $160 < D < 280$ km and $100 < D < 500$ km, respectively. Similarly, Fraser et al. (2014) found that dynamically quiescent ("cold") KBOs have a steeper bright-end slope than excited ("hot") KBOs, although the distinction vanishes in the faint end of the distribution.

The fact that the cold and hot populations are distinct in terms of spectral slope (Tegler & Romanishin, 2000; Doressoundiram et al. 2008), number of binary systems (Noll et

al. 2008 and this book), size and albedo (Vilenius et al. 2014), strengths the hypothesis that these two sub-populations had different dynamical histories and therefore formed in different regions of the planetary disk. These results are consistent with the Nice model (Batygin et al. 2011), indicating that hot Classical formed closer to the Sun compared to their present location and migrated during the early Solar System evolution, while the cold population formed in-situ.

4.2 Resonant

Thirty-seven resonant TNOs were investigated in the thermal wavelengths. Most of them (25) are Plutinos populating the 3:2 resonance with Neptune (Table 3). The Plutinos sizes range from about 85 km to 730 km for the largest body investigated (2003 AZ84), except the dwarf planet Pluto. Their albedos range from 4 to 28%, as reported in Mommert et al. (2012) and Lellouch et al. (2013), with a median (mean) value $p_V = 9\%$ ($11 \pm 6\%$) comparable to that of Centaurs, Jupiter family comets and other TNOs, excepting the detached and cold classicals. Mommert et al. (2012) found that the Plutino size distribution is reproduced using a cumulative power law with $q = 2$ at sizes ranging from 120-400 km and $q = 3$ at larger sizes. They did not find any correlation between the different physical parameters of the Plutinos, except a clear anti-correlation between eccentricity and diameter, likely caused by a discovery bias. Among the 18 Plutinos investigated in their study, six have evidence of water ice and show an higher albedo ($> 11\%$) than the average Plutino value.

The investigated outer resonants are brighter ($p_V = 16\%$ median and $15 \pm 7\%$ mean values) and bigger than Plutinos, very likely because of the discovery and selection biases. Their size ranges from ~ 150 km to ~ 1200 km for the largest body investigated, 2007 OR10 (Pál et al. 2016; Kiss et al. 2018), located in the 3:10 mean motion resonance with Neptune.

4.3 Detached/SDO population

The thermal properties were determined for 20 Scattered disk objects (SDO) and 8 Detached transneptunians (Table 3). Santos-Sanz et al. (2012) analyzed 15 scattered-disk/detached objects. They report that SDO are smaller than 400 km (excluding 2007 OR10, which is also classified as outer resonant), while detached objects are larger than 250 km, the larger size of the measured detached bodies being again a discovery/selection bias. Excluding the dwarf planet Eris, the two populations have different median (mean) albedos: 6% ($8 \pm 5\%$) for the SDOs, and 15% ($20 \pm 13\%$) for the detached bodies. Santos-Sanz et al. (2012) and Stansberry et al. (2008) proposed that larger objects have higher albedo because they may more easily retain volatiles. A possible positive correlation between albedo, size and perihelion distance was interpreted as a consequence of increased volatile sublimation and/or space weathering effects at low heliocentric distances, both of which leading to surface darkening.

4.4 Centaurs

Size, albedo and thermal properties were derived for 55 Centaurs combining the Spitzer, Herschel (and in some cases WISE) observations (Bauer et al. 2013; Duffard et al. 2014;

Tegler et al. 2016; Romanishin & Tegler 2018). Centaurs have a median (mean) albedo of 6% ($7 \pm 4\%$). Most of the Centaurs (92%) are smaller than ~ 120 km in diameter, and they are thought to be fragments from collisions of larger parent bodies (Pan & Sari 2005). Regarding sizes, Duffard et al. (2014) claim a lack of objects with sizes between 120 and 190 km, while the largest two, 2002 GZ₃₂ and Chariklo, reach $D \sim 240$ km. They further report a size dichotomy between red Centaurs, which are all small (< 120 km) and grey ones, which can reach ~ 240 km.

4.5 Haumea family

Haumea is in a weak 7:12 resonance with Neptune (Ragozzine & Brown 2007) and it is hypothesized to be the parent body of a TNO collisional family (Brown et al. 2007). Vilenius et al. (2018) found that the thermally detected Haumea family members have high albedos in the range ~ 0.3 - 0.8 (median $p_V = 0.48^{+0.28}_{-0.18}$), indicative for the presence of water ice. Deep water ice signatures are actually detected spectroscopically on Haumea, one of its moons (Hi'iaka) and several of the family members (see Brown et al. 2012). Also the cumulative size distribution for sizes in the range 175-300 km is steeper ($q=3.2^{+0.7}_{-0.4}$) than for dynamical interlopers¹⁶ with $D < 500$ km.

4.6 Colors/albedo correlations

A comprehensive study of the color-albedo distribution for 109 TNOs and Centaurs with available visible spectral slopes or colors and albedo values (see Table 3) was presented by Lacerda et al. (2014). They found that excluding the dwarf planet and the Haumea family members, the Transneptunian population is globally split in two clusters: the dark neutral and the bright red objects. The dark neutral group include spectrally gray objects, having an average spectral slope $S \sim 10\%/100$ nm and values $< 18\%/100$ nm, and low albedo values, clustered at $p_V \sim 5\%$. The red and bright objects have $18 < S < 58\%/100$ nm, and albedos $> 6\%$, with a higher median albedo value (around 15%). The dwarf planets and Haumea family members represent a third group of objects, having high albedo and small spectral slope values resulting from the presence of surface volatiles or exposed water ice.

The detailed analysis of spectral slope versus albedo for the different dynamical populations shows that Centaurs, Plutinos, hot Classicals and SDOs have objects in both groups, while cold Classicals, detached and outer resonants have only bright red TNOs (Lacerda et al. 2014). These results agree with conclusions from previous studies (that lacked the albedo information), finding that dynamically excited TNO populations are composed of two main types of surfaces (Fraser & Brown 2012, Bauer et al. 2013). This agrees with the scenario (Malhotra 1995; Gladman et al. 2002; Batygin et al. 2011) that cold Classicals, detached and outer resonants formed in distant regions from the Sun and that their bright red surfaces may be related to heliocentric-distance-dependent fractionation of surface volatiles with different sublimation temperatures (Brown et al.

¹⁶ Interlopers (as defined by Ragozzine & Brown 2007) belong to the same dynamical cluster as family members but lack the H₂O spectral features.

2011; Fraser & Brown 2012; Wong & Brown 2016), with methanol and/or hydrogen sulfide playing a key role¹⁷. Conversely, hot Classicals, Plutinos, Centaurs and SDOs, formed closer to the Sun and in a wider range of heliocentric distances, from 20 AU to about 48 AU (Petit et al. 2011), resulting in a wider range of physical properties, both in term of surface colors and albedo.

The color-albedo splitting in two groups is particularly prominent for Centaurs (Bauer et al. 2013, Duffard et al. 2014, Tegler et al. 2016, Romanishin & Tegler 2018) with median albedos of $\sim 5\%$ for the dark-neutral group and $\sim 8.4\%$ for the bright red, with the red group also having lower mean inclinations. An early explanation of the Centaur color bimodality in terms of collisional resurfacing has been invalidated by Thébaud & Doressoundiram (2003). Thermal processing has also been invoked (Melita & Licandro 2012) whereby red objects tend to spend shorter amount of times at small heliocentric distances; but in this case, Pholus would be a striking counter example. Romanishin & Tegler (2018) find that grey Centaurs have albedos not significantly different from those of the Trojans, consistent with a common origin.

5 Thermal and emissivity properties

5.1 Thermal inertia

In addition to size, shape and albedo, physical properties accessible to thermal measurements include thermal inertia, surface roughness and surface emissivity. Thermal inertia Γ is related to thermal conductivity κ through a relation that also involves the material density ρ and heat capacity C ($\Gamma = \sqrt{\kappa\rho C}$). The latter two parameters are usually unknown but as pointed out by Delbó et al. (2015), their plausible range of variation is much smaller than that for κ – which can vary by order of magnitudes between fine grain regolith and compact rock/ices. This justifies that Γ , the most directly accessible variable in a thermophysical model, be used as a proxy for κ , itself an indicator on the processes contributing to thermal conduction (intragrain, intergrain, or radiation-assisted heat transfer, e.g. Gundlach & Blum 2013; Ferrari & Lucas 2016).

Ensemble properties The unambiguous determination of an object’s thermal inertia requires good-quality spin- and shape information (e.g. Hanuš et al. 2018). Rotation periods have been measured for ~ 150 objects, but less than 10% of them have shapes and pole direction available. Therefore, the simple NEATM model still remains the default approach, when dealing with “large” samples. Although the typical NEATM accuracy is 15 % on diameter (Wolters & Green 2009), NEATM-based biases for asteroids occur mostly at large phase angle, a problem that is not relevant for TNOs/Centaurs. The NEATM-derived diameters usually agree with equivalent diameters from stellar occultation values to within much better accuracy (see Ortiz et al., same book). The beaming factor is then a proxy for the combined effect of thermal inertias, spin state and surface roughness. In rare cases where the thermal inertia is estimated, it characterizes the

¹⁷ We note that CH₃OH has been detected on a few objects, but H₂S has not so far (see chapter by Barucci and Merlin).

response of the object to the diurnal cycle and pertains to a layer comparable to the diurnal skin depth.

Lellouch et al. (2013) compiled (or re-derived) 85 beaming factors (η) values for TNOs/Centaurs to assess ensemble thermal inertia properties for the population. They found that: (i) beaming factors range from values < 1 to ~ 2.5 (close to the maximum value expected in the limit of high thermal inertia for an equator-on object); (ii) η values > 2 are lacking at small (< 30 AU) heliocentric distances; (iii) beaming factors lower than 1 occur frequently ($\sim 40\%$ of the objects), implying that surface roughness effects are important. Based on a statistical description of the bodies' spin properties and surface roughness, they determined that all these trends could be explained by a mean thermal inertia of $\Gamma = (2.5 \pm 0.5) \text{ J m}^{-2} \text{ s}^{-0.5} \text{ K}^{-1}$ (SI), with evidence for a decrease of Γ with increasing heliocentric distance r_h , corresponding to a power law $\Gamma \sim r_h^{-(1.0 \text{ to } 1.7)}$. Another finding was that high-albedo objects have preferentially lower thermal inertias.

Such thermal inertias are considerably smaller than for other Solar System icy bodies (e.g. $\Gamma = 50\text{-}70$ for Jupiter's satellites, $5\text{-}20$ SI for Saturn's (Howett et al. 2010 and references therein), $\Gamma = 10\text{-}25$ for Pluto/Charon, see below). They are also 2-3 orders of magnitude smaller than values for compact ices, typically $2000\text{-}2600$ SI (resp. $700\text{-}160$ SI) for crystalline (resp. amorphous) ice at $150\text{-}30$ K. Surface porosity and granularity strongly reduce the thermal conductivity, and are likely to be the cause of the measured low thermal inertias. Regarding the temperature dependence of the thermal inertia, Lellouch et al. (2013) noted that if thermal conduction is dominantly radiation-assisted (i.e. $\kappa \propto T^3$), Γ is expected to be nearly proportional to T^2 , i.e. r_h^{-1} . Based on a model of grain contact and radiative conduction, Ferrari & Lucas (2016) could quantitatively explain the low Γ values and their heliocentric distance if amorphous ice is present at cm depths below a thin layer of crystalline ice. The smaller value of Γ for "the mean TNO" compared e.g. to Pluto/Charon does not necessarily imply different regolith properties. Rather it may be related to different diurnal skin depths, which for equal density / thermal properties, is typically 4-5 times shallower on a 8 h-rotating TNO than on the 6.39 day period Pluto/Charon. This interpretation implies that the thermal inertia increases with depth, which is confirmed by recent estimates of the seasonal thermal inertia (Bertrand & Forget 2016).

Pluto/Charon and other prominent TNOs Thermal inertias of Pluto ($\Gamma = 16\text{-}26$ SI) and Charon ($\Gamma = 9\text{-}14$ SI) have been estimated based on unresolved thermal lightcurves of the system, observed by ISO, Spitzer and Herschel (Lellouch et al. 2000a, 2011, 2016), covering altogether $20\text{-}500 \mu\text{m}$. The pre-New Horizons Pluto model was described with three surface units (N_2 ice, CH_4 ice, and H_2O -tholin) and the determined thermal inertia globally applies to the non- N_2 ice (i.e. the non-isothermal) regions. The spatially-separated measurements of the cm/mm/submm brightness temperature ($T_B = 31\text{-}33$ K for Pluto vs $42\text{-}45$ K for Charon; Butler et al. 2015 and personnel communication) are consistent with estimated surface temperatures (Lellouch et al. 2011). The seemingly higher thermal inertia for Pluto vs Charon may result from a significant contribution of atmospheric conduction within a porous upper surface (Spencer & Moore 1992, Lellouch et al. 2000b).

At Pluto, the seasonal skin depth is 120 times larger than the diurnal skin depth for a given set of thermal properties. Determining the seasonal thermal inertia requires measurements over seasonal timescales, or at least a temperature value in the polar night (Leyrat et al. 2016). But an object’s sub-surface seasonal inertia also controls volatile cycles and the distribution of ices at a point in time (e.g. Young 2013). Bertrand & Forget (2016) found that Pluto’s pressure cycle, as well as the accumulation of N_2 and CO ices in the low-latitude Sputnik Planitia basin, can be explained by a seasonal thermal inertia $\Gamma_{seasonal} = (500-1500)$ SI, with 800 SI as the preferred value, corresponding to an annual skin depth of ~ 40 m.

Although Charon lacks an atmosphere, a somewhat similar reasoning may be used to constrain its seasonal thermal inertia. Grundy et al. (2016) interpret the red coloration of Charon’s poles as due to winter cold-trapping of methane gas escaping from Pluto’s atmosphere and captured by Charon, followed by photolytic processing of the material into more complex and less volatile molecules. For methane to be cold-trapped, Charon’s winter poles temperatures must fall below an estimated 25 K. This condition is met for a seasonal thermal inertia $\Gamma_{seasonal} = 2.5-40$ SI (i.e. comparable to the diurnal value), but conversely it implies some upper limit to $\Gamma_{seasonal}$, and it is likely that a value as high as the Pluto one would violate the constraint. These results (i) confirm the vertical variation of Pluto’s thermal inertia with depth (ii) suggest that Charon’s seasonal thermal inertia is smaller than Pluto’s, as is the case for the diurnal Γ .

For more details on the Pluto-Charon system and the interpretation of New Horizons measurements see also the chapters by Grundy et al. and Spencer et al. (same book).

Dwarf planet (136138) Haumea is the only other TNO with a definitely detected thermal lightcurve (Lellouch et al. 2010, Lockwood et al. 2014, Santos-Sanz et al. 2017; Müller et al. 2018). Shape information is also available from high-quality lightcurve observations (e.g. Lacerda et al. 2008), and most recently from stellar occultation, which also provides the pole orientation from the detection of a ring system (Ortiz et al. 2017). Adopting a shape model from Lacerda et al. (2008), Santos-Sanz et al. (2017) inferred an extremely small thermal inertia ($\Gamma < 0.5$ SI), essentially constrained by the lack of temporal shift between the optical and thermal lightcurves, and modelling the lightcurve amplitude then required a phase integral $q > 0.73$. After the occultation results, Müller et al. (2018) revisited the problem by (i) re-reducing the Herschel data; (ii) using the occultation-lightcurve derived 3-D size-spin-shape solution; (iii) estimating and correcting for the contribution of satellites and rings to the thermal flux. They reported a thermal inertia in the range 2-15 SI, with $\Gamma = 5$ SI as the most likely value. The higher value compared to the previous estimate results from the combination of (i) a strongly subdued lightcurve amplitude in the latest version of data reduction; (ii) the larger effective diameter and lower albedo yielded by the occultation results; (iii) the neglect of satellite/rings fluxes in the former study. In spite of the large difference, the new value for Γ is in light with the gross picture of low thermal inertia for the TNO population. Further reanalysis for Haumea might still be warranted in the light of the newly available value for q (0.45 from Verbiscer et al. 2018).

Thermal inertia results for other individual TNOs, derived from thermophysical models exploring parameter space (diameter, thermal inertia, roughness, spin state), are scarce. They are summarized in Table 2.

Table 2. Thermal inertia values for individual TNOs.

Object	Thermal inertia (SI)
Chiron	3-10 ⁽¹⁾ , 0-10 ⁽²⁾
Chariko	3-30 ⁽¹⁾ , 1.5-10 ⁽²⁾
Quaoar	2-10 ⁽¹⁾
Orcus	0.4-2 ⁽¹⁾
Bienor	6-20 ⁽²⁾
2007 UK ₁₂₆	0.7-10 ⁽³⁾
2013 AZ ₆₀	≥50 ⁽⁶⁾
2007 OR ₁₀	1-10 ⁽⁷⁾
Haumea	0-0.5 ⁽⁴⁾ , 2-15 ⁽⁵⁾
Pluto	16-26 ^(8,9)
Charon	9-14 ^(8,9)
Galilean satellites	50-70 ⁽¹⁰⁾
Saturnian satellites	5-20 ⁽¹⁰⁾

(1) Fornasier et al. 2013; (2) Lellouch et al. 2017;
(3) Schindler et al. 2017; (4) Santos-Sanz et al. 2017;
(5) Müller et al. 2018; (6) Pál et al. 2015;
(7) Kiss et al. 2018; (8,9) Lellouch et al. 2011/2016;
(10) Howett et al. 2010.

5.2 Emissivity

A factor impacting surface/sub-surface temperatures calculated either by NEATM or TPM is the so-called bolometric emissivity (ϵ_b). ϵ_b is defined as the Planck-function weighted average of the spectral emissivity $\epsilon(\lambda)$, where the latter is related to the spectral directional hemispheric reflectivity¹⁸. In addition, for a given surface/subsurface temperature profile, the radiation locally emitted at some wavelength depends on $\epsilon(\lambda)$. Many studies on asteroids have shown evidence for subdued fluxes at long wavelengths (submm/mm) compared to model expectations. This behaviour is usually termed “emissivity effect”, but quantitative estimates of this “emissivity” depend on how much physics is put in the reference model. For example, the increasing transparency of ices towards long wavelengths (see e.g. Mishima et al. 1983 for H₂O ice) implies that radiation progressively originates from the sub-surface. As dayside temperatures decrease with depth, this could lead one to misinterpret an apparent decline of the T_B with λ in terms of a lower “physical” emissivity. The mixing of horizontally variable surface temperatures has the same effect of decreasing T_B with λ (until the Rayleigh-Jeans limit is hit). Nonetheless, spectrally declining emissivities may also have physical causes. These

¹⁸ In asteroid science, ϵ_b is routinely taken as 0.9 on the basis that it is a typical value for silicates, given their mid-IR albedo. As extensively discussed by Myhrvold (2018), this assumption and other approximations of the NEATM are questionable, but we don’t dwell into this here.

include: (i) reflection of upward-propagating thermal radiation at the surface (often described by Fresnel reflection for a dielectric surface); (ii) particle scattering, which produces an emissivity minimum for particle sizes a comparable to $\lambda/4\pi$; (iii) volume scattering, a process in which subsurface inhomogeneities or voids on scales comparable or larger than the wavelength in weakly-absorbing medium cause multiple internal reflections (iv) thermal inertia increase with depth over the first \sim cm into the surface, as observed for the Moon regolith (Keihm 1984), Mercury (Mitchell & de Pater 1994) or asteroid 21 Lutetia (Gulkis et al. 2012).

These effects are still poorly characterized for TNOs. For Pluto/Charon, system-averaged T_B decline from ~ 53 K at $20 \mu\text{m}$ to ~ 35 K at $500 \mu\text{m}$ (Lellouch et al. 2016) and level out at this value across the mm/cm range (Butler et al. 2015, and in prep.). Lellouch et al. (2016) showed that 35 K is lower than any expected temperature for the dayside surface/subsurface of Pluto and Charon, and inferred a “true” spectral emissivity decreasing steadily from 1 at 20–25 μm to ~ 0.7 at $500 \mu\text{m}$. This kind of behavior is usually not observed in asteroids (when proper allowance is made for subsurface sound-ing, see Keihm et al. 2013), but is found in several outer solar system icy surfaces (e.g. Muhleman & Berge 1991; Ostro et al. 2006; Janssen et al. 2009; Le Gall et al. 2014; Ries & Janssen 2015) and in various kinds of ice and snow on Earth (Hewison & English 1999). Lellouch et al. (2016) concluded that the combination of a high dielectric constant ($\epsilon_r = 3\text{--}5$) and a considerable surface material transparency (typical penetration depth ~ 1 cm at $500 \mu\text{m}$) was responsible for the effect.

Similar studies, albeit less detailed, have been performed on a dozen other TNO or Centaurs. This includes (i) Herschel/SPIRE 250–500 μm measurements of 9 objects strongly detected with Herschel/PACS (Fornasier et al. 2013) (ii) ALMA observations of 4 objects at 0.87 and 1.30 mm (Brown & Butler 2017) and of six other at 1.30 mm only (Lellouch et al. 2017), complemented by ancient and less accurate but useful data from IRAM and JCMT. The SPIRE measurements generally did not detect the objects at $500 \mu\text{m}$ (and sometimes not at 350 or even $250 \mu\text{m}$), implying an emissivity decline at wavelengths $>200 \mu\text{m}$, but the derived emissivity curves are very uncertain. The much more accurate ALMA data show long-wavelength emissivity effects for all objects except Makemake, and lead to a mean *relative* radio emissivity ϵ_r (i.e. ratioed to the bolometric emissivity) of $\epsilon_r = 0.70 \pm 0.13$. Lellouch et al. (2017) demonstrated the importance of including proper shape models and accounting for variable spin orientation to infer these emissivities. No correlation was found between the radio emissivity and other (semi)-physical parameters such as diameter, color, composition, beaming factor, albedo, subsolar temperature, although a possible trend of increasing emissivity with grain size was suggested. A surprising result from Brown & Butler (2017) is the sometimes marked (but not in consistent directions) spectral variation of emissivity for some objects over 0.87–1.3 mm. This is unexpected because in the framework of scattering effects, the emissivity minimum at $\lambda \sim 4\pi a$ is expected to be broad due to particle size distribution.

6 Outlook

The Spitzer, WISE and Herschel missions provided a wealth of thermal data which was the key for the determination of thermophysical (sample-)properties of Centaurs and TNOs. But with the end of the Herschel mission in 2013 it is not possible right now to detect these objects close to their thermal emission peak in the far-IR regime. Individual objects can in principle be measured at mid-IR (e.g., with SOFIA, possibly also from ground), but only the brightest ones are detectable and with very little scientific gain over the existing observations from Spitzer and Herschel. In the submm/mm wavelength range the situation is more comfortable (e.g. with ALMA, IRAM), but measurements of a significant sample remain very time consuming. In addition, the unknowns about the objects' emissivity make the interpretation more challenging. The next big step in thermal emission observations of TNOs is expected to come with JWST¹⁹. Norwood et al. (2016) stated that MIRI²⁰ will be capable to characterize the thermal emission of TNOs in the 18-25 μm filters. Parker et al. (2016a) expect that the MIRI measurements will resolve ambiguities in the thermophysical model studies and constrain thermal inertia and roughness of TNO surfaces. JWST will also see the short-wavelengths thermal emission excess related to hotter terrains (low-albedo regions) or originating from dark satellites. In combination with existing Spitzer and Herschel measurements, the JWST thermal emission measurements will lead to a significant refinement of the radiometric size-albedo solutions and possibly provide evidence for seasonal volatile transport (e.g. on Sedna). A major contribution to the thermal studies of Centaurs and TNOs is expected to come with the Space Infrared Telescope for Cosmology and Astrophysics (SPICA). It will cover the far-IR regime, but with much better sensitivity compared to Spitzer or Herschel. However, the launch of this JAXA/ESA-proposed mission would not be before 2032.

Acknowledgement

The research leading to these results has received funding from the European Union's Horizon 2020 Research and Innovation Programme, under Grant Agreement no. 687378.

¹⁹ James Webb Space Telescope: <https://jwst.stsci.edu>

²⁰ Mid-Infrared Instrument: <https://jwst.stsci.edu/instrumentation/miri>

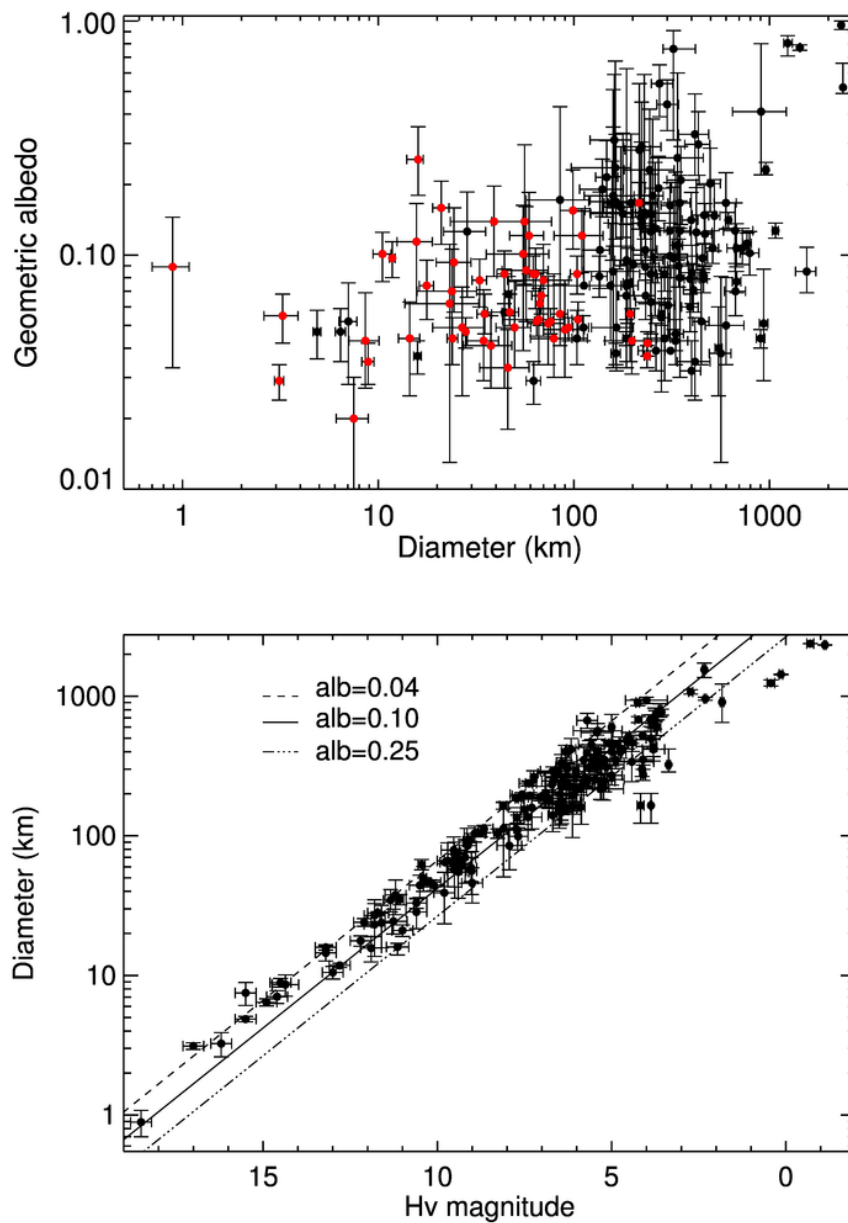


Fig. 1. Top: Geometric albedo versus diameter for 170 TNOs (in black) and Centaurs (in red) from Herschel, Spitzer, and WISE data (see Table 3, but excluding objects with upper/lower limit estimates). The selection bias due to distance is clearly visible as small sizes are measured only for closer bodies, i.e. Centaurs. Bottom: Diameter versus H_v magnitude for 170 TNOs and Centaurs. Absolute magnitude with an albedo of 10% is a good proxy for size for the majority of TNOs.

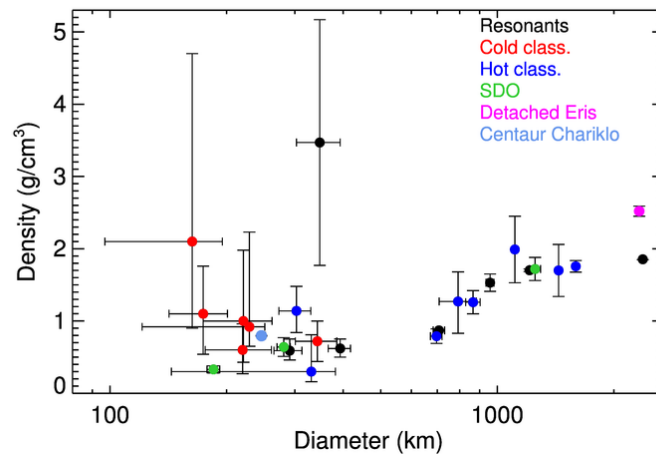


Fig. 2. Bulk density versus the effective diameter for the observed TNOs. Red symbols - cold classicals; blue symbols - hot Classicals; black symbols - resonants; green symbols - SDO; magenta symbol-detached. Density values are from the references given in the text, as well as a description of the outliers. We add also Pluto & Charon from New Horizons mission results.

Table 3: Absolute magnitude used in the modelling and derived radiometric diameters, geometric albedos, and beaming factor for TNOs and Centaurs. The individual fluxes and the criteria for the dynamical classification for the objets are available in the TNOs are Cool public database: <http://public-tnosarecool.lesia.obspm.fr/Published-observations.html>. "med/out res" refers to resonants beside plutinos, not including Haumea and family members. Geometric albedo and Absolute magnitude are given in the V filter, except for the 2 objects 2003 FE128 and 2007 RW10*; binary systems; †: absolute magnitude and albedo are in the R band; §: fixed η ; References: a) Duffard et al. 2014; b) Pal et al. 2015; c) Fornasier et al. 2013; d) Fornasier et al. 2014; e) Lacerda et al. 2014; f) Vilenius et al. 2014; g) Vilenius et al. 2012; h) Lellouch et al. 2013; i) Mommert, 2013 PhD thesis; j) Vilenius et al. 2018; k) Mommert et al. 2012; l) Kiss et al. 2018; m) Müller et al. 2010; n) Kiss et al. 2013; o) Santos-Sanz et al. 2012; p) Stansberry et al. 2008; q) Bauer et al. 2013; r) Nimmo et al. 2017; s) Buratti et al. 2015; t) Buratti et al. 2017; u) Stern et al. 2018; in cases where the uncertainty for H-mag is unknown, we assumed 0.3 mag.

Object	Dyn. class	H _v	Diam. (km)	p _v	η	Ref.
2000 GM137	Centaur	14.36±0.38	8.6 ^{+1.5} _{-1.5}	0.043 ^{+0.026} _{-0.016}	§ 1.20 ^{+0.35} _{-0.35}	a
2004 QQ26	Centaur	9.53±0.36	79.0 ^{+19.0} _{-19.0}	0.044 ^{+0.039} _{-0.014}	§ 1.20 ^{+0.35} _{-0.35}	a
2013 AZ60	Centaur/SDO	10.45±0.10	62.3 ^{+5.3} _{-5.3}	0.029 ^{+0.006} _{-0.006}	1.70 ^{+0.90} _{-0.90}	b
(2060) Chiron	Centaur	5.92±0.20	215.6 ^{+9.9} _{-9.9}	0.167 ^{+0.037} _{-0.030}	0.95 ^{+0.09} _{-0.10}	c
(5145) Pholus	Centaur	7.68±0.28	99.0 ^{+15.0} _{-14.0}	0.155 ^{+0.076} _{-0.049}	0.77 ^{+0.16} _{-0.16}	a
(7066) Nessus	Centaur	9.51±0.22	57.0 ^{+17.0} _{-14.0}	0.086 ^{+0.075} _{-0.034}	§ 1.20 ^{+0.35} _{-0.35}	a
(8405) Asbolus	Centaur	9.13±0.25	85.0 ^{+8.0} _{-9.0}	0.056 ^{+0.019} _{-0.015}	0.97 ^{+0.14} _{-0.18}	a
(10199) Chariklo	Centaur	7.40±0.25	238.0 ^{+10.0} _{-10.0}	0.042 ^{+0.005} _{-0.005}	1.12 ^{+0.14} _{-0.14}	c, d
(10370) Hylonome	Centaur	9.51±0.08	74.0 ^{+16.0} _{-16.0}	0.051 ^{+0.030} _{-0.017}	1.29 ^{+0.31} _{-0.31}	a
(31824) Elatus	Centaur	10.40±0.09	49.8 ^{+10.4} _{-9.8}	0.049 ^{+0.028} _{-0.016}	§ 1.20 ^{+0.35} _{-0.35}	a
(32532) Theus	Centaur	9.40±0.16	62.0 ^{+3.0} _{-3.0}	0.083 ^{+0.016} _{-0.013}	0.87 ^{+0.08} _{-0.08}	a
(52872) Okyrhoe	Centaur	11.07±0.10	35.0 ^{+3.0} _{-3.0}	0.056 ^{+0.012} _{-0.010}	0.71 ^{+0.12} _{-0.13}	a
(52975) Cyllarus	Centaur	9.02±0.15	56.0 ^{+21.0} _{-18.0}	0.139 ^{+0.157} _{-0.064}	§ 1.20 ^{+0.35} _{-0.35}	a
(54598) Bienor	Centaur	7.57±0.34	198.0 ^{+6.0} _{-7.0}	0.043 ^{+0.016} _{-0.012}	1.58 ^{+0.07} _{-0.07}	a
(55576) Amycus	Centaur	8.27±0.11	104.0 ^{+8.0} _{-8.0}	0.083 ^{+0.016} _{-0.015}	1.00 ^{+0.12} _{-0.13}	a
(60558) Echeclus	Centaur	9.78±0.14	64.6 ^{+1.6} _{-1.6}	0.052 ^{+0.007} _{-0.007}	0.86 ^{+0.04} _{-0.04}	a
(63252) 2001 BL41	Centaur	11.34±0.21	34.6 ^{+6.6} _{-6.1}	0.043 ^{+0.028} _{-0.014}	§ 1.20 ^{+0.35} _{-0.35}	a
(83982) Crantor	Centaur	9.03±0.16	59.0 ^{+11.0} _{-12.0}	0.121 ^{+0.064} _{-0.038}	§ 1.20 ^{+0.35} _{-0.35}	a
(95626) 2002 GZ32	Centaur	7.37±0.10	237.0 ^{+8.0} _{-8.0}	0.037 ^{+0.004} _{-0.004}	0.97 ^{+0.05} _{-0.07}	a
(119315) 2001 SQ73	Centaur	9.15±0.11	90.0 ^{+23.0} _{-20.0}	0.048 ^{+0.030} _{-0.018}	§ 1.20 ^{+0.35} _{-0.35}	a
(119976) 2002 VR130	Centaur	11.26±0.39	24.4 ^{+5.4} _{-4.6}	0.093 ^{+0.066} _{-0.036}	§ 1.20 ^{+0.35} _{-0.35}	a
(120061) 2003 CO1	Centaur	9.07±0.05	94.0 ^{+5.0} _{-5.0}	0.049 ^{+0.005} _{-0.006}	1.23 ^{+0.12} _{-0.11}	a
(136204) 2003 WL7	Centaur	8.75±0.16	105.0 ^{+6.0} _{-7.0}	0.053 ^{+0.010} _{-0.010}	1.02 ^{+0.07} _{-0.05}	a
(145486) 2005 UJ438	Centaur	11.14±0.32	16.0 ^{+1.0} _{-2.0}	0.256 ^{+0.097} _{-0.076}	0.34 ^{+0.09} _{-0.08}	a
(248835) 2006 SX368	Centaur	9.45±0.11	76.0 ^{+2.0} _{-2.0}	0.052 ^{+0.007} _{-0.006}	0.87 ^{+0.04} _{-0.06}	a
(250112) 2002 KY14	Centaur	10.37±0.07	47.0 ^{+3.0} _{-4.0}	0.057 ^{+0.011} _{-0.007}	§ 1.20 ^{+0.35} _{-0.35}	a
(281371) 2008 FC76	Centaur	9.44±0.10	68.0 ^{+6.0} _{-7.0}	0.067 ^{+0.017} _{-0.011}	§ 1.20 ^{+0.35} _{-0.35}	a
(447178) 2005 RO43	Centaur	7.34±0.51	194.0 ^{+10.0} _{-10.0}	0.056 ^{+0.036} _{-0.021}	1.12 ^{+0.05} _{-0.08}	a
2000 CN105	Cold classical	5.20±0.30	247.0 ^{+63.0} _{-40.0}	0.151 ^{+0.070} _{-0.059}	§ 1.20 ^{+0.35} _{-0.35}	e
2001 QS322	Cold classical	6.91±0.68	186.0 ^{+99.0} _{-24.0}	0.095 ^{+0.531} _{-0.060}	§ 1.20 ^{+0.35} _{-0.35}	f
2001 RZ143	Cold classical	6.69±0.13	140.0 ^{+39.0} _{-33.0}	0.191 ^{+0.066} _{-0.045}	0.75 ^{+0.23} _{-0.19}	g
2001 XR254	Cold classical	6.05±0.15	221.0 ^{+41.0} _{-71.0}	0.136 ^{+0.168} _{-0.044}	§ 1.20 ^{+0.35} _{-0.35}	f
2003 QR91*	Cold classical	6.55±0.56	280.0 ^{+27.0} _{-30.0}	0.054 ^{+0.035} _{-0.028}	1.20 ^{+0.10} _{-0.12}	f
2003 WU188	Cold classical	5.96±0.64	< 220	> 0.15	1.20 ^{+0.35} _{-0.35}	f
(66652) Borasisi*	Cold classical	6.121±0.07	163.0 ^{+32.0} _{-66.0}	0.236 ^{+0.438} _{-0.077}	0.77 ^{+0.19} _{-0.47}	f
(79360) Sila-Nunam	Cold classical	5.56±0.04	343.0 ^{+42.0} _{-42.0}	0.090 ^{+0.027} _{-0.017}	1.36 ^{+0.21} _{-0.19}	g

Continued on next page

Table 3 – continued from previous page

Object	Dyn. class	H_V	Diam. (km)	p_V	η	Ref.
(88611) Teharonhiawako	Cold classical	6.00±0.13	220.0 ^{+41.0} _{-44.0}	0.145 ^{+0.086} _{-0.045}	1.08 ^{+0.30} _{-0.28}	f
(119951) 2002 KX14	Cold classical	4.86±0.10	455.0 ^{+27.0} _{-27.0}	0.097 ^{+0.014} _{-0.013}	1.79 ^{+0.16} _{-0.15}	g
(120181) 2003 UR292	Cold classical	7.40±0.40	136.0 ^{+16.0} _{-26.0}	0.105 ^{+0.081} _{-0.033}	§ 1.20 ^{+0.35} _{-0.35}	f
(135182) 2001 QT322	Cold classical	7.29±0.67	159.0 ^{+30.0} _{-47.0}	0.085 ^{+0.424} _{-0.052}	§ 1.20 ^{+0.35} _{-0.35}	f
(275809) 2001 QY297	Cold classical	5.86±0.31	229.0 ^{+22.0} _{-108.0}	0.152 ^{+0.439} _{-0.035}	1.52 ^{+0.22} _{-0.92}	f
(385266) 2001 QB298	Cold classical	6.10±0.30	196.0 ^{+71.0} _{-53.0}	0.167 ^{+0.162} _{-0.082}	§ 1.20 ^{+0.35} _{-0.35}	i
(385437) 2003 GH55	Cold classical	6.43±0.12	178.0 ^{+21.0} _{-56.0}	0.150 ^{+0.182} _{-0.031}	§ 1.20 ^{+0.35} _{-0.35}	f
(469438) 2002 GV31	Cold classical	6.10±0.60	<180.0	>0.019	§ 1.20 ^{+0.35} _{-0.35}	f
(469514) 2003 QA91*	Cold classical	5.76±0.63	260.0 ^{+30.0} _{-36.0}	0.130 ^{+0.119} _{-0.075}	0.83 ^{+0.10} _{-0.15}	f
(469705) 2005 EF298	Cold classical	6.40±0.50	174.0 ^{+27.0} _{-32.0}	0.160 ^{+0.130} _{-0.070}	§ 1.20 ^{+0.35} _{-0.35}	g
(508869) 2002 VT130	Cold classical	5.80±0.30	324.0 ^{+57.0} _{-68.0}	0.097 ^{+0.098} _{-0.049}	§ 1.20 ^{+0.35} _{-0.35}	i
1996 TS66	Hot classical	6.50±0.05	159.0 ^{+44.0} _{-46.0}	0.179 ^{+0.173} _{-0.070}	0.75 ^{+0.21} _{-0.27}	f
2001 KA77	Hot classical	5.64±0.12	310.0 ^{+70.0} _{-60.0}	0.099 ^{+0.052} _{-0.056}	2.52 ^{+0.18} _{-0.83}	g
2001 QC298	Hot classical	6.26±0.32	303.0 ^{+27.0} _{-30.0}	0.061 ^{+0.027} _{-0.017}	0.99 ^{+0.08} _{-0.10}	f
2001 QD298	Hot classical	6.71±0.17	233.0 ^{+27.0} _{-63.0}	0.067 ^{+0.062} _{-0.014}	§ 1.26 ^{+0.35} _{-0.35}	g
2002 GH32	Hot classical	6.58±0.28	<180	>0.13	§ 1.26 ^{+0.35} _{-0.35}	f
(19308) 1996 TO66	Hot classical	4.81±0.14	<330.0	>0.200	§ 1.74 ^{+0.17} _{-0.17}	j
(19521) Chaos	Hot classical	5.00±0.06	600.0 ^{+140.0} _{-130.0}	0.050 ^{+0.030} _{-0.016}	2.20 ^{+1.20} _{-1.10}	g
(20000) Varuna	Hot classical	3.76±0.035	668.0 ^{+154.0} _{-86.0}	0.127 ^{+0.040} _{-0.042}	2.18 ^{+1.04} _{-0.49}	h
(24835) 1995 SM55	Hot classical	4.49±0.035	<280.0	>0.360	§ 1.74 ^{+0.17} _{-0.17}	j
(35671) 1998 SN165	Hot classical	5.707±0.085	393.0 ^{+39.0} _{-38.0}	0.060 ^{+0.019} _{-0.013}	§ 1.23 ^{+0.35} _{-0.35}	g
(50000) Quaoar*	Hot classical	2.73±0.06	1073.6 ^{+37.9} _{-37.9}	0.127 ^{+0.010} _{-0.009}	1.73 ^{+0.08} _{-0.08}	c
(55565) 2002 AW197	Hot classical	3.57±0.05	768.0 ^{+39.0} _{-38.0}	0.112 ^{+0.012} _{-0.011}	1.29 ^{+0.13} _{-0.10}	f
(55636) 2002 TX300	Hot classical	3.37±0.05	323.0 ^{+95.0} _{-37.0}	0.760 ^{+0.180} _{-0.450}	1.80 ^{+0.50} _{-0.90}	j
(55637) 2002 UX25*	Hot classical	3.87±0.02	697.2 ^{+23.0} _{-24.5}	0.107 ^{+0.008} _{-0.008}	1.07 ^{+0.05} _{-0.05}	h
(78799) 2002 XW93	Hot classical	5.40±0.70	565.0 ^{+71.0} _{-73.0}	0.038 ^{+0.043} _{-0.025}	0.79 ^{+0.27} _{-0.24}	g
(86177) 1999 RY215	Hot classical	7.235±0.093	263.0 ^{+29.0} _{-37.0}	0.039 ^{+0.012} _{-0.007}	§ 1.20 ^{+0.35} _{-0.35}	g
(90568) 2004 GV9	Hot classical	4.23±0.10	680.0 ^{+34.0} _{-34.0}	0.077 ^{+0.008} _{-0.008}	1.93 ^{+0.09} _{-0.07}	g
(120178) 2003 OP32	Hot classical	4.10±0.07	274.0 ^{+47.0} _{-25.0}	0.540 ^{+0.110} _{-0.150}	§ 1.74 ^{+0.17} _{-0.17}	j
(120347) Salacia*	Hot classical	4.25±0.05	901.0 ^{+45.0} _{-45.0}	0.044 ^{+0.004} _{-0.004}	1.16 ^{+0.03} _{-0.03}	l
(136108) Haumea*	Hot classical	0.43±0.11	1239.5 ^{+68.7} _{-57.8}	0.804 ^{+0.062} _{-0.095}	0.95 ^{+0.33} _{-0.26}	c
(136472) Makemake	Hot classical	0.14±0.05	1430.0 ^{+9.0} _{-9.0}	0.770 ^{+0.020} _{-0.020}	2.29 ^{+0.46} _{-0.40}	h
(138537) 2000 OK67	Hot classical	6.47±0.13	164.0 ^{+33.0} _{-45.0}	0.169 ^{+0.159} _{-0.052}	§ 1.20 ^{+0.35} _{-0.35}	f
(145452) 2005 RN43	Hot classical	3.89±0.05	679.0 ^{+55.0} _{-73.0}	0.107 ^{+0.029} _{-0.018}	§ 1.20 ^{+0.35} _{-0.35}	g
(145453) 2005 RR43	Hot classical	4.13±0.08	300.0 ^{+43.0} _{-34.0}	0.440 ^{+0.120} _{-0.100}	§ 1.74 ^{+0.17} _{-0.17}	j
(148780) Altjira*	Hot classical	6.44±0.14	331.0 ^{+51.0} _{-187.0}	0.043 ^{+0.183} _{-0.009}	1.62 ^{+0.24} _{-0.83}	f
(174567) Varda*	Hot classical	3.61±0.05	792.0 ^{+91.0} _{-84.0}	0.102 ^{+0.024} _{-0.020}	0.84 ^{+0.28} _{-0.22}	f
(182934) 2002 GJ32	Hot classical	6.16±0.13	416.0 ^{+81.0} _{-78.0}	0.035 ^{+0.019} _{-0.011}	2.05 ^{+0.38} _{-0.36}	f
(202421) 2005 UQ513	Hot classical	3.87±0.14	498.0 ^{+63.0} _{-75.0}	0.202 ^{+0.084} _{-0.049}	§ 1.27 ^{+0.35} _{-0.35}	g
(230965) 2004 XA192	Hot classical	4.42±0.63	339.0 ^{+20.0} _{-95.0}	0.260 ^{+0.340} _{-0.150}	0.62 ^{+0.79} _{-0.49}	f
(307251) 2002 KW14	Hot classical	5.88±0.11	161.0 ^{+35.0} _{-40.0}	0.310 ^{+0.281} _{-0.094}	§ 1.20 ^{+0.35} _{-0.35}	f
(307261) 2002 MS4	Hot classical	4.00±0.60	934.0 ^{+47.0} _{-47.0}	0.051 ^{+0.036} _{-0.022}	1.06 ^{+0.06} _{-0.06}	g
(307616) 2003 QW90	Hot classical	5.00±0.30	401.0 ^{+63.0} _{-48.0}	0.084 ^{+0.026} _{-0.022}	§ 1.11	e
(416400) 2003 UZ117	Hot classical	5.23±0.15	222.0 ^{+57.0} _{-42.0}	0.290 ^{+0.160} _{-0.110}	§ 1.74 ^{+0.17} _{-0.17}	j
(444030) 2004 NT33	Hot classical	4.74±0.11	423.0 ^{+87.0} _{-80.0}	0.125 ^{+0.069} _{-0.039}	0.69 ^{+0.460} _{-0.32}	f
(469306) 1999 CD158	Hot classical	5.35±0.67	<310.0	>0.130	§ 1.20 ^{+0.35} _{-0.35}	j

Continued on next page

Table 3 – continued from previous page

Object	Dyn. class	H_V	Diam. (km)	p_V	η	Ref.
(469615) 2004 PT107	Hot classical	6.33±0.11	400.0 ^{+45.0} _{-51.0}	0.032 ^{+0.011} _{-0.007}	§ 1.53 ^{+0.35} _{-0.35}	f
2001 KD77	Plutino	6.42±0.08	232.3 ^{+40.5} _{-39.4}	0.089 ^{+0.044} _{-0.027}	§ 1.20 ^{+0.35} _{-0.35}	k
2002 XV93	Plutino	5.42±0.46	549.2 ^{+21.7} _{-23.0}	0.040 ^{+0.020} _{-0.015}	1.24 ^{+0.06} _{-0.06}	k
2003 UT292	Plutino	6.85±0.68	185.6 ^{+17.9} _{-18.0}	0.067 ^{+0.068} _{-0.034}	§ 1.20 ^{+0.35} _{-0.35}	k
(15820) 1994 TB	Plutino	7.934±0.354	85.0 ^{+36.0} _{-28.0}	0.172 ^{+0.258} _{-0.097}	1.260 ^{+0.97} _{-0.65}	h
(15875) 1996 TP66	Plutino	7.51±0.09	154.0 ^{+28.8} _{-33.7}	0.074 ^{+0.063} _{-0.031}	§ 1.20 ^{+0.35} _{-0.35}	k
(28978) Ixion	Plutino	3.83±0.04	617.0 ^{+19.0} _{-20.0}	0.141 ^{+0.011} _{-0.011}	0.91 ^{+0.04} _{-0.06}	h
(33340) 1998 VG44	Plutino	6.67±0.04	248.0 ^{+43.0} _{-41.0}	0.063 ^{+0.026} _{-0.017}	1.55 ^{+0.58} _{-0.38}	h
(38628) Huya*	Plutino	5.04±0.03	458.0 ^{+9.2} _{-9.2}	0.083 ^{+0.004} _{-0.004}	0.93 ^{+0.02} _{-0.02}	c
(47171) 1999 TC36*	Plutino	5.41±0.10	393.1 ^{+25.2} _{-26.8}	0.079 ^{+0.013} _{-0.011}	1.10 ^{+0.07} _{-0.08}	k
(47932) 2000 GN171	Plutino	6.45±0.34	147.1 ^{+20.7} _{-17.8}	0.215 ^{+0.093} _{-0.070}	1.11 ^{+0.24} _{-0.21}	k
(55638) 2002 VE95	Plutino	5.70±0.06	249.8 ^{+13.5} _{-13.1}	0.149 ^{+0.019} _{-0.016}	1.40 ^{+0.12} _{-0.11}	k
(84719) 2002 VR128	Plutino	5.58±0.37	448.5 ^{+42.1} _{-43.2}	0.052 ^{+0.027} _{-0.018}	§ 1.20 ^{+0.35} _{-0.35}	k
(84922) 2003 VS2	Plutino	4.11±0.38	523.0 ^{+35.1} _{-34.4}	0.147 ^{+0.063} _{-0.043}	1.57 ^{+0.30} _{-0.23}	k
(90482) Orcus*	Plutino	2.31±0.03	958.4 ^{+22.9} _{-22.9}	0.231 ^{+0.018} _{-0.011}	0.97 ^{+0.05} _{-0.02}	c
(120216) 2004 EW95	Plutino	6.69±0.35	291.1 ^{+20.3} _{-25.9}	0.044 ^{+0.021} _{-0.015}	§ 1.20 ^{+0.35} _{-0.35}	k
(120348) 2004 TY364	Plutino	4.52±0.07	512.0 ^{+37.0} _{-40.0}	0.107 ^{+0.020} _{-0.015}	1.55 ^{+0.15} _{-0.10}	h
(133067) 2003 FB128	Plutino	6.80±0.30	186.0 ^{+27.0} _{-29.0}	0.074 ^{+0.035} _{-0.021}	§ 1.20 ^{+0.35} _{-0.35}	e
(144897) 2004 UX10	Plutino	4.75±0.16	398.1 ^{+32.6} _{-39.3}	0.141 ^{+0.044} _{-0.031}	§ 1.20 ^{+0.35} _{-0.35}	k
(175113) 2004 PF115	Plutino	4.54±0.25	468.2 ^{+38.6} _{-49.1}	0.123 ^{+0.043} _{-0.033}	§ 1.20 ^{+0.35} _{-0.35}	k
(208996) 2003 AZ84*	Plutino	3.74±0.08	727.0 ^{+61.9} _{-66.5}	0.107 ^{+0.023} _{-0.016}	1.05 ^{+0.19} _{-0.15}	k
(307463) 2002 VU130	Plutino	5.47±0.83	252.9 ^{+33.6} _{-31.3}	0.179 ^{+0.202} _{-0.103}	§ 1.20 ^{+0.35} _{-0.35}	k
(450265) 2003 WU172	Plutino	6.30±0.30	312.0 ^{+0.0} _{-0.0}	0.039 ^{+0.000} _{-0.000}	§ 2.60 ^{+0.35} _{-0.35}	e
(455502) 2003 UZ413	Plutino	5.70±0.30	670.0 ^{+84.0} _{-82.0}	0.070 ^{+0.022} _{-0.015}	§ 1.20 ^{+0.35} _{-0.35}	e
(469372) 2001 QF298	Plutino	5.43±0.07	408.2 ^{+40.2} _{-44.9}	0.071 ^{+0.020} _{-0.014}	§ 1.20 ^{+0.35} _{-0.35}	k
(469987) 2006 HJ123	Plutino	5.32±0.66	216.4 ^{+29.7} _{-34.2}	0.281 ^{+0.259} _{-0.152}	§ 1.20 ^{+0.35} _{-0.35}	k
(126154) 2001 YH140	med res	5.80±0.20	349.0 ^{+81.0} _{-81.0}	0.080 ^{+0.050} _{-0.050}	§ 1.20 ^{+0.35} _{-0.35}	m
2002 GP32	out res	6.90±0.30	201.0 ^{+25.0} _{-29.0}	0.091 ^{+0.061} _{-0.024}	§ 1.20 ^{+0.35} _{-0.35}	e
(26308) 1998 SM165	out res	6.02±0.08	291.0 ^{+22.0} _{-26.0}	0.083 ^{+0.018} _{-0.013}	1.55 ^{+0.11} _{-0.10}	h
(26375) 1999 DE9	out res	5.16±0.05	311.0 ^{+29.0} _{-32.0}	0.163 ^{+0.041} _{-0.026}	0.71 ^{+0.10} _{-0.11}	h
(42301) 2001 UR163	out res	4.10±0.30	352.0 ^{+85.0} _{-53.0}	0.209 ^{+0.082} _{-0.074}	§ 1.20 ^{+0.35} _{-0.35}	e
(82075) 2000 YW134	out res	4.88±0.05	<500	>0.08	§ 1.20 ^{+0.35} _{-0.35}	m
(84522) 2002 TC302	out res	4.17±0.10	584.1 ^{+105.6} _{-88.0}	0.115 ^{+0.047} _{-0.033}	1.09 ^{+0.37} _{-0.25}	c
(119979) 2002 WC19*	out res	4.88±0.07	348.0 ^{+45.0} _{-45.0}	0.167 ^{+0.052} _{-0.037}	1.12 ^{+0.16} _{-0.17}	h
(143707) 2003 UY117	out res	5.70±0.30	247.0 ^{+30.0} _{-29.0}	0.126 ^{+0.039} _{-0.028}	§ 1.20 ^{+0.35} _{-0.35}	e
(225088) 2007 OR10*	out res	2.34±0.05	1252.0 ^{+43.0} _{-42.0}	0.13 ^{+0.01} _{-0.01}	1.20 ^{+0.35} _{-0.35}	l
(308379) 2005 RS43	out res	5.00±0.30	271.0 ^{+45.0} _{-40.0}	0.193 ^{+0.071} _{-0.053}	§ 1.20 ^{+0.35} _{-0.35}	e
(469505) 2003 FE128	out res	¶ 6.30±0.30	157.0 ^{+60.0} _{-7.0}	¶ 0.167 ^{+0.085} _{-0.072}	§ 1.20 ^{+0.35} _{-0.35}	f
(471143) 2010 EK139	out res	3.80±0.10	433.0 ^{+63.0} _{-64.0}	0.297 ^{+0.113} _{-0.078}	0.60 ^{+0.33} _{-0.25}	h
2012 DR30	SDO	7.04±0.35	188.0 ^{+9.4} _{-9.4}	0.076 ^{+0.031} _{-0.025}	0.81 ^{+0.074} _{-0.062}	n
(15874) 1996 TL66	SDO	5.39±0.12	339.0 ^{+20.0} _{-20.0}	0.110 ^{+0.021} _{-0.015}	1.15 ^{+0.08} _{-0.05}	o
(26181) 1996 GQ21	SDO	5.20±0.30	349.0 ^{+43.0} _{-49.0}	0.127 ^{+0.043} _{-0.026}	§ 1.20 ^{+0.35} _{-0.35}	i
(29981) 1999 TD10	SDO	8.93±0.30	103.7 ^{+13.6} _{-13.5}	0.044 ^{+0.014} _{-0.010}	1.64 ^{+0.32} _{-0.31}	p
(42355) Typhon*	SDO	7.72±0.04	185.0 ^{+7.0} _{-7.0}	0.044 ^{+0.003} _{-0.003}	1.48 ^{+0.07} _{-0.07}	o
(44594) 1999 OX3	SDO	7.72±0.09	135.0 ^{+13.0} _{-12.0}	0.081 ^{+0.018} _{-0.015}	1.04 ^{+0.27} _{-0.22}	h
(48639) 1995 TL8*	SDO	5.29±0.06	244.0 ^{+82.0} _{-63.0}	0.231 ^{+0.189} _{-0.102}	1.38 ^{+0.80} _{-0.49}	h

Continued on next page

Table 3 – continued from previous page

Object	Dyn. class	H_V	Diam. (km)	p_V	η	Ref.
(65489) Ceto*	SDO	6.54±0.06	281.0 ^{+11.0} _{-11.0}	0.056 ^{+0.006} _{-0.006}	1.04 ^{+0.05} _{-0.05}	o
(73480) 2002 PN34	SDO	8.66±0.03	112.0 ^{+7.0} _{-7.0}	0.049 ^{+0.006} _{-0.006}	1.02 ^{+0.07} _{-0.09}	o
(82158) 2001 FP185	SDO	6.39±0.07	332.0 ^{+31.0} _{-24.0}	0.046 ^{+0.007} _{-0.007}	1.23 ^{+0.24} _{-0.19}	o
(127546) 2002 XU93	SDO	8.11±0.10	164.0 ^{+9.0} _{-9.0}	0.038 ^{+0.004} _{-0.004}	1.12 ^{+0.05} _{-0.08}	o
(309239) 2007 RW10	SDO	¶6.39±0.61	247.0 ^{+30.0} _{-30.0}	¶0.083 ^{+0.068} _{-0.039}	§1.20 ^{+0.35} _{-0.35}	o
(40314) 1999 KR16	Detached	6.24±0.15	232.0 ^{+34.0} _{-36.0}	0.105 ^{+0.049} _{-0.027}	§1.20 ^{+0.35} _{-0.35}	j
(90377) Sedna	Detached	1.83±0.05	906.0 ^{+14.0} _{-258.0}	0.410 ^{+0.390} _{-0.190}	0.72 ^{+0.78} _{-0.54}	h
(120132) 2003 FY128	Detached	5.09±0.09	460.0 ^{+21.0} _{-21.0}	0.079 ^{+0.010} _{-0.010}	1.07 ^{+0.08} _{-0.08}	o
(136199) Eris*	Detached	-1.12±0.03	2326.0 ^{+12.0} _{-12.0}	0.960 ^{+0.040} _{-0.040}	0.87 ^{+0.26} _{-0.41}	h
(145480) 2005 TB190	Detached	4.40±0.11	464.0 ^{+62.0} _{-62.0}	0.148 ^{+0.051} _{-0.036}	§1.20 ^{+0.35} _{-0.35}	o
(229762) 2007 UK126	Detached	3.69±0.10	599.0 ^{+77.0} _{-77.0}	0.167 ^{+0.058} _{-0.038}	§1.20 ^{+0.35} _{-0.35}	o
(303775) 2005 QU182	Detached	3.80±0.32	416.0 ^{+73.0} _{-73.0}	0.328 ^{+0.160} _{-0.109}	§1.20 ^{+0.35} _{-0.35}	o
(470316) 2007 OC10	Detached	5.43±0.10	309.0 ^{+37.0} _{-37.0}	0.127 ^{+0.040} _{-0.028}	§1.20 ^{+0.35} _{-0.35}	o
(330759) 2008 SO218	Centaur	12.8±0.3	11.8 ± 0.4	0.097 ± 0.017	0.823 ± 0.046	q
2008 JS14	Centaur	13.2±0.3	14.5 ± 1.8	0.044 ± 0.019	1.046 ± 0.186	q
2010 CR140	Centaur	15.5±0.3	7.5 ± 1.4	0.020 ± 0.01	1.111 ± 0.283	q
2010 HU20	Centaur	13.0±0.3	10.513± 1.1	0.101 ± 0.024	0.976 ± 0.162	q
2010 LG61	Centaur	18.5±0.3	0.89 ± 0.19	0.089 ± 0.056	1.00 ± 0.400	q
2010 OR1	Centaur	16.2±0.3	3.25 ± 0.64	0.055 ± 0.013	0.831 ± 0.146	q
2010 OM101	Centaur	17. ±0.3	3.12 ± 0.17	0.029 ± 0.005	1.054 ± 0.105	q
2010 PO58	Centaur	14.5±0.3	8.88 ± 0.63	0.035 ± 0.007	0.915 ± 0.093	q
167P/CINEOS	Centaur	9.7±0.3	66.17 ± 22.9	0.053 ± 0.019	0.8 ± 0.360	q
29P/Schwassm.-W. 1	Centaur	9. ±0.3	46. ± 13.	0.033 ± 0.015	0.64 ± 0.29	q
(148975) 2001 XA255	Centaur	11.2±0.3	37.7 ± 10.5	0.041 ± 0.014	0.703 ± 0.186	q
(309139) 2006 XQ51	Centaur	9.8±0.3	39.1 ± 15.7	0.139 ± 0.058	0.8 ± 0.456	q
(310071) 2010 KR59	Centaur	7.7±0.3	110.06 ± 30.82	0.121 ± 0.037	0.8 ± 0.324	q
(309737) 2008 SJ236	Centaur	12.2±0.3	17.7 ± 1.5	0.074 ± 0.021	0.800 ± 0.110	q
(328884) 2010 LJ109	Centaur	10.1±0.3	44.2 ± 3.8	0.083 ± 0.021	0.748 ± 0.103	q
(332685) 2009 HH36	Centaur	10.6±0.3	33.0 ± 2.8	0.078 ± 0.018	0.739 ± 0.095	q
(342842) 2008 YB3	Centaur	9.5±0.3	67.1 ± 1.0	0.062 ± 0.012	0.839 ± 0.012	q
(346889) 2009 QV38	Centaur	11.8±0.3	23.2 ± 9.5	0.062 ± 0.049	0.8 ± 0.389	q
2007 VH305	Centaur	11.6±0.3	23.8 ± 8.0	0.070 ± 0.036	0.8 ± 0.384	q
2008 HY21	Centaur	12.1±0.3	24.0 ± 1.5	0.044 ± 0.010	1.22 ± 0.094	q
2010 BL4	Centaur	11.9±0.3	15.7 ± 3.2	0.114 ± 0.052	0.8 ± 0.333	q
2010 ES65	Centaur	11.8±0.3	26.9 ± 7.9	0.049 ± 0.024	0.8 ± 0.28	q
2010 FH92	Centaur	11.7±0.3	28.0 ± 0.6	0.047 ± 0.007	0.730 ± 0.023	q
2010 RM64	Centaur	11.0±0.3	21.0 ± 2.0	0.159 ± 0.048	0.85 ± 0.144	q
2010 TH	Centaur	9.2±0.3	69.9 ± 24.2	0.078 ± 0.033	0.8 ± 0.363	q
2011 MM4	Centaur	9.3±0.3	63.7 ± 6.2	0.083 ± 0.024	0.841 ± 0.119	q
2005 VJ119	SDO	10.6±0.3	28.5 ± 6.9	0.126 ± 0.060	0.8 ± 0.30	q
2010 BK118	SDO	10.2±0.3	46.4 ± 1.8	0.068 ± 0.013	0.821 ± 0.043	q
2010 GW64	SDO	14.9±0.3	6.42 ± 0.38	0.047 ± 0.012	0.795 ± 0.075	q
2010 GW147	SDO	13.2±0.3	15.9 ± 0.7	0.037 ± 0.006	0.869 ± 0.056	q
2010 JH124	SDO	14.6±0.3	7.04 ± 0.74	0.052 ± 0.024	0.959 ± 0.164	q
C/2010 KW7 (WISE)	SDO	15.5±0.3	4.87 ± 0.22	0.047 ± 0.011	0.75 ± 0.06	q
2010 WG9	SDO	8.1±0.3	112.7 ± 61.9	0.074 ± 0.080	0.8 ± 0.423	q

Continued on next page

Table 3 – continued from previous page

Object	Dyn. class	H_v	Diam. (km)	p_v	η	Ref.
(336756) 2010 NV1	SDO	10.5 ± 0.3	44.2 ± 8.0	0.057 ± 0.030	0.661 ± 0.168	q
C/2011 KP36 (Spacewatch)	Centaur	9.4 ± 0.3	55.1 ± 19.4	0.101 ± 0.062	0.8 ± 0.4	q
Pluto	Plutino	-0.7	2376.6 ± 3.2	0.52 ± 0.03 (0.08-1.0)		r,s,t
Charon	Plutino	1.0	1212.0 ± 1.0	0.41 ± 0.02 (0.11-0.73)		t,u

References

- Altenhoff, W. J. & Stumpff, P. 1995. Size estimate of "asteroid" 2060 chiron from 250GHz measurements. *A&A* 293, L41-L42.
- Altenhoff, W. J., Menten, K. M. & Bertoldi, F. 2001. Size determination of the Centaur Chariklo from millimeter-wavelength bolometer observations. *A&A* 366, L9-L12.
- Altenhoff, W. J., Bertoldi, F. & Menten, K. M. 2004. Size estimates of some optically bright KBOs. *A&A* 415, 771-775.
- Aumann, H. H. & Walker, R. G. 1987. IRAS observations of the Pluto-Charon system. *AJ* 94, 1088-1091.
- Barr, A.C., Schwamb, M. E. 2016. Interpreting the densities of the Kuiper belt's dwarf planets. *MNRAS* 460, 1542-1548.
- Barucci, M. A., Merlin, F., Perna, D., Alvarez-Candal, A., Müller, T., Mommert, M. et al. 2012. The extra red plutino (55638) 2002 VE95. *A&A* 539, A152, 6 pp.
- Batygin, K., Brown, M. E., & Fraser, W. C. 2011. Retention of a Primordial Cold Classical Kuiper Belt in an Instability-Driven Model of Solar System Formation. *ApJ* 738, 13, 8pp.
- Bauer, J. M., Grav, T., Blauvelt, E., Mainzer, A. K., Masiero, J. R., Stevenson, R. et al. 2013. Centaurs and Scattered Disk Objects in the Thermal Infrared: Analysis of WISE/NEOWISE Observations. *ApJ* 773, 22, 11pp.
- Bertoldi, F., Altenhoff, W., Weiss, A., Menten, K. M. & Thum, C. 2006. The trans-neptunian object UB313 is larger than Pluto. *Nature* 439, 563-564.
- Bertrand, T. & Forget, F. 2016. Observed glacier and volatile distribution on Pluto from atmosphere-topography processes. *Nature* 540, 86-89.
- Bowell, E., Hapke, B., Domingue, D., Lumme, K., Peltoniemi, J., Harris, A. W. 1989. Application of photometric models to asteroids. In: Asteroids II; Proceedings of the Conference, Tucson, AZ, Mar. 8-11, 1988. Univ. of Arizona Press, p524-556.
- Braga-Ribas, F., Sicardy, B., Ortiz, J. L., Snodgrass, C., Roques, F., Vieira-Martins, R. et al. 2014. A ring system detected around the Centaur (10199) Chariklo. *Nature* 508, 72-75.
- Brown, M. E., Trujillo, C. & Rabinowitz, D. 2004. Discovery of a Candidate Inner Oort Cloud Planetoid. *ApJ* 617, 645-649.
- Brown, M. E. & Schaller, E. L. 2007. The Mass of Dwarf Planet Eris. *Science* 316, 1585.
- Brown, M. E., Schaller, E. L., Fraser, W. C. 2011. A Hypothesis for the Color Diversity of the Kuiper Belt. *ApJ* 739, L60, 5pp.
- Brown, M. E., Schaller, E. L., Fraser, W. C. 2012. Water Ice in the Kuiper Belt. *AJ* 143, 146, 7pp.
- Brown, M. E. 2013. The Density of Mid-sized Kuiper Belt Object 2002 UX25 and the Formation of the Dwarf Planets. *ApJL* 778, L34, 5pp.
- Brown, M. E. & Butler, B. J. 2017. The Density of Mid-sized Kuiper Belt Objects from ALMA Thermal Observations. *AJ* 154, 19, 7pp.
- Brown, M. E. & Butler, B. J. 2018. Medium-sized satellites of large Kuiper belt objects. *arXiv:1801.07221*.
- Brown, R. H. 1985. Ellipsoidal geometry in asteroid thermal models - The standard radiometric model. *Icarus* 64, 53-63.
- Brucker, M. J., Grundy, W. M., Stansberry, J. A., Spencer, J. R., Sheppard, S. S., Chiang, E. I., Buie, M. W. 2009. High albedos of low inclination Classical Kuiper belt objects. *Icarus* 201, 284-294.
- Butler, B. J., Gurwell, M., Lellouch, E., Moullet, A., Moreno, R., Bockelee-Morvan, D. et al. 2015. Long Wavelength Observations of Thermal Emission from Pluto and Charon with ALMA. DPS meeting # 47, id.210.04.
- Buratti, B. J., Hicks, M. D., Dalba, P. A., Chu, D., O'Neill, A., Hillier, J. K. et al. 2015. Photometry of Pluto 2008-2014: Evidence of ongoing seasonal volatile transport and activity. *ApJL* 804, L6, 6pp.
- Buratti, B. J., Hofgartner, J. D., Hicks, M. D., Weaver, H. A., Stern, S. A., Momary, T. et al. 2017. Global albedos of Pluto and Charon from LORRI New Horizons observations. *Icarus* 287, 207-217.
- Campins, H., Telesco, C. M., Osip, D. J., Rieke, G. H., Rieke, M. J., Schulz, B. 1994. The color temperature of (2060) Chiron: A warm and small nucleus. *AJ* 108, 2318-2322.
- Cruikshank, D. P., Stansberry, J. A., Emery, J. P., Fernández, Y. R., Werner, M. W., Trilling, D. E. et al. 2005. The High-Albedo Kuiper Belt Object (55565) 2002 AW197. *ApJ* 624, L53-L56.
- Cruikshank, D. P., Stansberry, J. A., Emery, J. P., van Cleve, J., Fernández, Y. R., Werner, M. W. et al. 2006. Solar System Observations with Spitzer Space Telescope. in *The Spitzer Space Telescope: New Views of the Cosmos*, Proceedings ASP Conference Series 357, 9-12 November, 2004 in Pasadena, California, USA. Edited by L. Armus and W.T. Reach. San Francisco: Astronomical Society of the Pacific, 2006., p.23.
- Davies, J. R., Spencer, J., Sykes, M., Tholen, D., Green, S. 1993. (5145) Pholus. *IAU Circ.*, No. 5698, #2 (1993).

Davies, J. R. 2000. Physical Characteristics of Trans-Neptunian Objects and Centaurs. in *Minor Bodies in the Outer Solar System: Proceedings of the ESO Workshop Held at Garching, Germany, 2-5 Nov 1998*. Edited by A. Fitzsimmons, D. Jewitt, and R.M. West. Springer-Verlag, 2000, p9.

Delbo' M., Mueller, M., Emery, J. P., Rozitis, B., Capria, M. T. 2015. Asteroid Thermophysical Modeling. in *Asteroids IV*, Patrick Michel, Francesca E. DeMeo, and William F. Bottke (eds.), University of Arizona Press, Tucson, 895 pp. ISBN: 978-0-816-53213-1, p.107-128.

Dias-Oliveira, A., Sicardy, B., Ortiz, J. L., Braga-Ribas, F., Leiva, R., Vieira-Martins, R. et al. 2017. Study of the Plutino Object (208996) 2003 AZ84 from Stellar Occultations: Size, Shape, and Topographic Features. *AJ* 154, 22, 13pp.

Doressoundiram, A., Boehnhardt, H., Tegler, S. C., Trujillo, C. 2008. Color Properties and Trends of the Transneptunian Objects. in: *The Solar System Beyond Neptune*, ed. M. A. Barucci, H. Boehnhardt, D. Cruikshank, A. Morbidelli, University of Arizona Press, Tucson, 592pp, 91-104.

Duffard, R., Pinilla-Alonso, N., Santos-Sanz, P., Vilenius, E., Ortiz, J. L., Müller, T. et al. 2014. TNOs are Cool: A Survey of the Transneptunian Region: A Herschel-PACS view of 16 Centaurs. *A&A* 564, A92, 17 pp.

Fernández, Y. R., Jewitt, D. C. & Sheppard, S. S. 2002. Thermal Properties of Centaurs Asbolus and Chiron. *AJ* 123, 1050-1055.

Ferrari, C. & Lucas, A. 2016. Low thermal inertias of icy planetary surfaces. Evidence for amorphous ice? *A&A* 588, A133, 14 pp.

Fornasier, S., Lellouch, E., Müller, T., Santos-Sanz, P., Panuzzo, P., Kiss, C. et al. 2013. TNOs are Cool program: combined observations of 9 Centaurs and TNOs with PACS and SPIRE instruments onboard the Herschel space telescope. *A&A* 555, A15, 22pp.

Fornasier, S., Lazzaro, D., Alvarez-Candal, A., Snodgrass, C., Tozzi, G. P., Carvano, J. M. et al. 2014. The Centaur 10199 Chariklo: investigation into rotational period, absolute magnitude, and cometary activity. *A&A* 568, L11, 5 pp.

Fraser, W.C. & Brown, M.E. 2012. The Hubble Wide Field Camera 3 Test of Surfaces in the Outer Solar System: The Compositional Classes of the Kuiper Belt. *AJ* 749, 33, 21 pp.

Fraser, W.C., Brown, M.E., Morbidelli, A., Parker, A., Batygin, K. 2014. The Absolute Magnitude Distribution of Kuiper Belt Objects. *ApJ* 782, 100, 14 pp.

Gerdes, D. W., Sako, M., Hamilton, S., Zhang, K., Khain, T., Becker, J. C. et al. 2017. Discovery and Physical Characterization of a Large Scattered Disk Object at 92 au. *ApJ Letters* 839, L15, 7 pp.

Gladman, B., Holman, M., Grav, T., Kavelaars, J., Nicholson, P., Aksnes, K. et al. 2002. Evidence for an Extended Scattered Disk. *Icarus* 157, 269-279.

Gladman, B., Marsden, B. G., VanLaerhoven, C. 2008. Nomenclature in the outer Solar System, in: *The Solar System Beyond Neptune*, ed. M. A. Barucci, H. Boehnhardt, D. Cruikshank, A. Morbidelli, University of Arizona Press, Tucson, 592pp, 43-57.

Grossin, O., Lamy, P. & Jorda, L. 2004. Properties of the nuclei of Centaurs Chiron and Chariklo. *A&A* 413, 1163-1175.

Grundy, W. M., Noll, K. S., Stephens, D. C. 2005. Diverse albedos of small trans-neptunian objects. *Icarus* 176, 184-191.

Grundy, W. M., Stansberry, J. A., Noll, K. S., Stephens, D. C., Trilling, D. E., Kern, S. D. et al. 2007. The orbit, mass, size, albedo, and density of (65489) Ceto/Phorcys: A tidally-evolved binary Centaur. *Icarus* 191, 286-297.

Grundy, W. M., Noll, K. S., Virtanen, J., Muinonen, K., Kern, S. D., Stephens, D. C. et al. 2008. (42355) Typhon Echidna: Scheduling observations for binary orbit determination. *Icarus* 197, 260-268.

Grundy, W. M., Cruikshank, D. P., Gladstone, G. R., Howett, C. J. A., Lauer T. R., Spencer, J. R. et al. 2016. The formation of Charon's red poles from seasonally cold-trapped volatiles. *Nature* 539, 65-68.

Gulkis, S., Keihm, S., Kamp, L., Lee, S., Hartogh, P., Crovisier, J. et al. 2012. Continuum and spectroscopic observations of asteroid (21) Lutetia at millimeter and submillimeter wavelengths with the MIRO instrument on the Rosetta spacecraft. *P&SS* 66, 31-42.

Gundlach, B. & Blum, J. 2013. A new method to determine the grain size of planetary regolith. *Icarus*, 223 479-492.

Hanuš, J., Delbo, M., Durech, J., Alí-Lagoa, V. 2018. Thermophysical modeling of main-belt asteroids from WISE thermal data. *Icarus*, 309, 297-337.

Harris, A. W. 1998. A Thermal Model for Near-Earth Asteroids. *Icarus* 131, 291-301.

Hewison, T. J. & English, S. J. 1999. Airborne retrievals of snow and ice surface emissivity at millimeter wavelengths. *IEEE Trans. Geosc. Remot. Sound.* 37, 1871-1879.

Howell, E., Marcialis, R., Cutri, R., Nolan, M., Lebofsky, L., Sykes, M. 1992. 1992 AD. *IAU Circ.*, No. 5449, #2 (1992). Edited by Green, D. W. E.

Howett, C. J. A., Spencer, J. R., Pearl, J., Segura, M. 2010. Thermal inertia and bolometric Bond albedo values for Mimas, Enceladus, Tethys, Dione, Rhea and Iapetus as derived from Cassini/CIRS measurements. *Icarus* 206, 573-593.

Janssen, M. A., Lorenz, R. D., West, R., Paganelli, F., Lopes, R. M., Kirk, R. L. et al. 2009. Titan's surface at 2.2-cm wavelength imaged by the Cassini RADAR radiometer: Calibration and first results. *Icarus* 200, 222-239.

Jewitt, D. & Luu, J. 1992. Submillimeter continuum observations of 2060 Chiron. *AJ* 104, 398-404.

Jewitt, D. 1994. Heat from Pluto. *AJ* 107, 372-378.

Jewitt, D. & Kalas, P. 1998. Thermal Observations of Centaur 1997 CU26. *ApJ* 499, L103-L106.

Jewitt, D., Ausseil, H., Evans, A. 2001. The size and albedo of the Kuiper-belt object (20000) Varuna. *Nature* 411, 446-447.

Jewitt, D. 2009. The Active Centaurs. *AJ* 137, 4296-4312.

Keihm, S. J. 1984. Interpretation of the lunar microwave brightness temperature spectrum - Feasibility of orbital heat flow mapping. *Icarus* 60, 568-589.

Keihm, S., Kamp, L., Gulkis, S., Hofstadter, M., Lee, S., Janssen, M., Choukroun, M. 2013. Reconciling main belt asteroid spectral flux density measurements with a self-consistent thermophysical model. *Icarus* 226, 1086-1102.

Kiss, Cs., Szabó, G., Horner, J., Conn, B. C., Müller, T. G., Vilenius, E., Sarneczky, K. et al. 2013. A portrait of the extreme solar system object 2012 DR30. *A&A* 555, A3, 13 pp.

Kiss, C., Pál, A., Farkas-Takács, A. I., Szabó, G. M., Szabó, R., Kiss, L. L., Molnár, L. et al. 2016. Nereid from space: rotation, size and shape analysis from K2, Herschel and Spitzer observations. *MNRAS* 457, 2908-2917.

Kiss, C., Marton, G., Farkas-Takács, A., Stansberry, J., Müller, T., Vinkó, J. et al. 2017. Discovery of a satellite of the large trans-Neptunian object (225088) 2007 OR10. *ApJL* 838, L1, 5 pp.

Kiss, Cs., Marton, G., Parker, A. H., Grundy, W., Farkas-Takács, A., Stansberry, J. et al. 2018. The mass and density of the dwarf planet (225088) 2007 OR 10. *Icarus*, submitted.

Kovalenko, I. D., Doressoundiram, A., Lellouch, E., Vilenius, E., Müller, T., Stansberry, J., 2017. "TNOs are Cool": A survey of the trans-Neptunian region. XIII. Statistical analysis of multiple trans-Neptunian objects observed with Herschel Space Observatory. *A&A* 608, A19, 8 pp.

Lacerda, P., Jewitt, D., Peixinho, N. 2008. High-Precision Photometry of Extreme KBO 2003 EL61. *AJ* 135, 1749-1756.

Lacerda, P., Fornasier, S., Lellouch, E., Kiss, C., Vilenius, E., Santos-Sanz, P. et al. 2014. TNOs Are Cool: A survey of the transneptunian region. XII. The albedo-color diversity of transneptunian objects. *ApJL* 793, L2, 6 pp.

Lagerros, J. S. V. 1996. Thermal physics of asteroids. I. Effects of shape, heat conduction and beaming. *A&A* 310, 1011-1020.

Lagerros, J. S. V. 1997. Thermal physics of asteroids. III. Irregular shapes and albedo variegations. *A&A* 325, 1226-1236.

Lagerros, J. S. V. 1998. Thermal physics of asteroids. IV. Thermal infrared beaming. *A&A* 332, 1123-1132.

Lebofsky, L. A., Tholen, D. J., Rieke, G. H., Lebofsky, M. J. 1984. 2060 Chiron: Visual and thermal infrared observations. *Icarus* 60, 532-537.

Le Gall, A., Leyrat, C., Janssen, M. A., Keihm, S., Wye, L. C., West, R. et al. 2014. Iapetus' near surface thermal emission modeled and constrained using Cassini RADAR Radiometer microwave observations. *Icarus* 241, 221-238.

Leiva, R., Sicardy, B., Camargo, J.L.B., Ortiz, J. L., Desmars, J., Bérard, D. et al. 2017. Size and Shape of Chariklo from Multi-epoch Stellar Occultations. *AJ* 154, 159, 23pp.

Lellouch, E., Laureijs, R., Schmitt, B., Quirico, E., de Bergh, C., Crovisier, J., Coustenis, A. 2000a. Pluto's Non-isothermal Surface. *Icarus* 147, 220-250.

Lellouch, E., Paubert, G., Moreno, R., Schmitt, B. 2000b. NOTE: Search for Variations in Pluto's Millimeter-Wave Emission. *Icarus* 147, 580-584.

Lellouch, E., Moreno, R., Ortiz, J. L., Paubert, G., Doressoundiram, A., Peixinho, N. 2002. Coordinated thermal and optical observations of Trans-Neptunian object (20000) Varuna from Sierra Nevada. *A&A* 391, 1133-1139.

Lellouch, E., Kiss C., Santos-Sanz P., Müller T. G., Fornasier S., Groussin, O. et al. 2010. TNOs are cool: A survey of the trans-Neptunian region. II. The thermal lightcurve of (136108) Haumea. *A&A* 518, L147, 5 pp.

Lellouch, E., Stansberry, J., Emery, E., Grund, W., Cruikshank, D. P. 2011. Thermal properties of Pluto's and Charon's surfaces from Spitzer observations. *Icarus* 214, 701-716.

Lellouch, E., Santos-Sanz, P., Lacerda, P., Mommert, M., Duffard, R., Ortiz, et al. 2013. "TNOs are Cool": A survey of the trans-Neptunian region. IX. Thermal properties of Kuiper belt objects and Centaurs from combined Herschel and Spitzer observations. *A&A* 557, A60, 19pp.

Lellouch, E., Santos-Sanz, P., Fornasier, S., Lim, T., Stansberry, J., Vilenius, E. et al. 2016. The long-wavelength thermal emission of the Pluto-Charon system from Herschel observations. Evidence for emissivity effect. *A&A* 588, id.A2, 15 pp.

Lellouch, E., Moreno, R., Müller, T., Fornasier, S., Santos-Sanz, P., Moullet, A. et al. 2017. The thermal emission of Centaurs and trans-Neptunian objects at millimeter wavelengths from ALMA observations. *A&A*, 608, id. A45, 21 pp.

Leyrat, C., Lorenz, R. D., Le Gall, A. 2016. Probing Pluto's underworld: Ice temperatures from microwave radiometry decoupled from surface conditions. *Icarus* 268, 50-55.

Lim T. L., Stansberry J., Müller T. G., Mueller, M., Lellouch, E., Kiss, C. et al. 2010. TNOs are Cool: A survey of the trans-Neptunian region. III. Thermophysical properties of 90482 Orcus and 136472 Makemake. *A&A* 518, L148, 5 pp.

Lockwood, A. C., Brown, M. E., Stansberry, J. 2014. The Size and Shape of the Oblong Dwarf Planet Haumea. *Earth, Moon and Planets* 111, 127-137.

Malhotra, R. 1995. The Origin of Pluto's Orbit: Implications for the Solar System Beyond Neptune. *AJ* 110, 420-429.

Margot, J. L., Trujillo, C., Brown, M. E., Bertoldi, F. 2002. The size and albedo of KBO 2002 AW197. *DPS Meeting #34*, id.17.03; *BAAS* 34, p.871.

Marton, G., Kiss, Cs., Balog, Z., Lellouch, E., Verebelyi, E., Klaas, U. 2015. Search for signatures of dust in the Pluto-Charon system using Herschel/PACS observations. *A&A* 579, L9, 5 pp.

Melita, M.D. & Licandro, J. 2012. Links between the dynamical evolution and the surface color of the Centaurs. *A&A* 539, A144, 6 pp.

Mishima, O., Klug, D. D., & Whalley, E. 1983. The far-infrared spectrum of ice Ih in the range 8-25 cm⁻¹. Sound waves and difference bands, with application to Saturn's rings. *J. Chem. Phys.* 78, 6399-6404.

Mitchell, D. L. & de Pater, I. 1994. Microwave imaging of Mercury's thermal emission at wavelengths from 0.3 to 20.5 cm. *Icarus* 110, 2-32.

Mommert, M., Harris, A. W., Kiss, C., Pál, A., Santos-Sanz, P., Stansberry, J. et al. 2012. TNOs are cool: A survey of the trans-Neptunian region. V. Physical characterization of 18 Plutinos using Herschel-PACS observations. *A&A* 541, A93, 17 pp.

Mommert M. 2013. Remnant Planetesimals and their Collisional Fragments: Physical Characterization from Thermal Infrared Observations. *Freie Universität Berlin*, PhD thesis, 300pp.

Moullet, A., Lellouch, E., Moreno, R., Gurwell, M. 2011. Physical studies of Centaurs and Trans-Neptunian Objects with the Atacama Large Millimeter Array. *Icarus* 213, 382-392.

Müller, T. G. & Lagerros, J. S. V. 1998. Asteroids as far-infrared photometric standards for ISOPHOT. *A&A* 338, 340-352.

Müller, T. G. & Lagerros, J. S. V. 2002. Asteroids as calibration standards in the thermal infrared for space observatories. *A&A* 381, 324-339.

Müller, T. G., Lellouch, E., Bönhardt, H., Stansberry, J., Barucci, A., Crovisier, J. et al. 2009. TNOs are Cool: A Survey of the Transneptunian Region. *EMP* 105, 209-219.

Müller T. G., Lellouch E., Stansberry J., Kiss, C., Santos-Sanz, P., Vilenius, E., et al. 2010. TNOs are Cool: A survey of the trans-Neptunian region. I. Results from the Herschel science demonstration phase (SDP). *A&A* 518, L146, 5 pp.

Müller, T., Kiss, Cs., Ali-Lagoa, V., Ortiz, J. L., Lellouch, E., Santos-Sanz, P. et al. 2018. Haumea's thermal emission revisited in the light of the occultation results. *Icarus*, submitted.

Muhleman, D. O., & Berge, G. L. 1991. Observations of Mars, Uranus, Neptune, Io, Europa, Ganymede, and Callisto at a wavelength of 2.66 MM. *Icarus* 92, 263-272.

Myhrvold, N. 2018. Asteroid thermal modeling in the presence of reflected sunlight. *Icarus* 303, 91-113.

Nimmo, F., Umurhan, O.; Lisse, C. M., Bierson, C. J., Lauer, T. R.; Buie, M. W. et al. 2017. Mean radius and shape of Pluto and Charon from New Horizons images. *Icarus* 287, 12-29.

Noll, K. S., Grundy, W. M., Stephens, D. C., Levison, H. F., Kern, S. D. 2008. Evidence for two populations of classical transneptunian objects: The strong inclination dependence of classical binaries. *Icarus* 194, 758-768.

Norwood, J., Hammel, H., Milam, S., Stansberry, J., Lunine, J. Chanover, N. et al. 2016. Solar System Observations with the James Webb Space Telescope. *PASP* 128:025004 (34pp).

Ortiz, J. L., Sota, A., Moreno, R., Lellouch, E., Biver, N., Doressoundiram, A. et al. 2004. A study of Trans-Neptunian object 55636 (2002 TX300). *A&A* 420, 383-388.

Ortiz, J., Sicardy, B., Braga-Ribas, F., Alvarez-Candal, A., Lellouch, E., Duffard, R. et al. 2012. Albedo and atmospheric constraints of dwarf planet Makemake from a stellar occultation. *Nature* 491, 566-569.

Ortiz, J. L., Duffard, R., Pinilla-Alonso, N., Alvarez-Candal, A., Santos-Sanz, P., Morales, N. et al. 2015. Possible ring material around centaur (2060) Chiron. *A&A* 576, A18, 12pp.

Ortiz, J. L., Santos-Sanz, P., Sicardy, B., Benedetti-Rossi, G., Bérard, D., Morales, N. et al. 2017. The size, shape, density and ring of the dwarf planet Haumea from a stellar occultation. *Nature* 550, 219-223.

Ostro, S. J., West, R. D., Janssen, M. A., Lorenz, R. D., Zebker, H. A., Black, G. J. et al. 2006. Cassini RADAR observations of Enceladus, Tethys, Dione, Rhea, Iapetus, Hyperion, and Phoebe. *Icarus* 183, 479-490.

Pätzold, M., Andert, T., Hahn, M., Asmar, S. W., Barriot, J.-P., Bird, M. K. 2016. A homogeneous nucleus for comet 67P/Churyumov-Gerasimenko from its gravity field. *Nature* 530, 63-65.

Pál, A., Kiss, C., Müller, T. G., Santos-Sanz, P., Vilenius, E., Szalai, N. et al. 2012. "TNOs are Cool": A survey of the trans-Neptunian region. VII. Size and surface characteristics of (90377) Sedna and 2010 EK139. *A&A* 541, L6, 4 pp.

Pál, A., Kiss, C., Horner, J., Szakats, R., Vilenius, E., Müller, T. et al. 2015. Physical properties of the extreme Centaur and super-comet candidate 2013 AZ60. *A&A* 583, A93, 8 pp.

Pál, A., Kiss, C., Müller, T., Molnar, L., Szabo, R., Szabo, G. M. et al. 2016. Large Size and Slow Rotation of the Trans-Neptunian Object (225088) 2007 OR10. Discovered from Herschel and K2 Observations. *AJ* 151, 117, 8 pp.

Pan, M. & Sari, R. 2005. Shaping the Kuiper belt size distribution by shattering large but strengthless bodies. *Icarus* 173, 342-348.

Parker, A., Pinilla-Alonso, N., Santos-Sanz, P., Stansberry, J., Alvarez-Candal, A., Bannister, M. et al. 2016a. Physical Characterization of TNOs with the James Webb Space Telescope. *PASP* 128:018010 (6pp).

Parker, A. H., Buie, M. W., Grundy, W. M., Noll, K. S. 2016b. Discovery of a Makemakean Moon. *ApJL* 825, L9, 5 pp.

Petit, J.-M., Kavelaars, J. J., Gladman, B. J., Jones, R. L., Parker, J. W., Van Laerhoven, C. et al. 2011. The Canada-France Ecliptic Plane Survey Full Data Release: The Orbital Structure of the Kuiper Belt. *AJ* 142, 131, 24pp.

Preusker, F., Scholten, F., Matz, K.-D., Roatsch, T., Hviid, S. F., Mottola, S. et al. 2017. The global meter-level shape model of comet 67P/Churyumov-Gerasimenko. *A&A* 607, L1, 5pp.

Ragozzine, D. & Brown, M. E. 2007. Candidate Members and Age Estimate of the Family of Kuiper Belt Object 2003 EL61. *AJ* 134, 2160-2167.

Ries, P. A. & Janssen, M. 2015. A large-scale anomaly in Enceladus' microwave emission. *Icarus* 257, 88-102.

Romanishin, W. & Tegler, S.C. 2018. Albedos of Centaurs, Jovian Trojans, and Hildas. *AJ* 156, 19, 11 pp.

Santos-Sanz P., Lellouch E., Fornasier S., Kiss C., Pal A., Müller T. G. 2012. TNOs are Cool: A Survey of the Transneptunian Region IV. Size/albedo characterization of 15 scattered disk and detached objects observed with Herschel Space Observatory-PACS. *A&A* 541, A92, 18 pp.

Santos-Sanz, P., Lellouch, E., Groussin, O., Lacerda, P., Müller, T. G., Ortiz, J. L. et al. 2017. "TNOs are Cool": A survey of the trans-Neptunian region. XII. Thermal light curves of Haumea, 2003 VS2 and 2003 AZ84 with Herschel/PACS. *A&A* 604, A95, 19 pp.

Schindler, K., Wolf, J., Bardecker, J., Olsen, A., Müller, T., Kiss, C. et al. 2017. Results from a triple chord stellar occultation and far-infrared photometry of the trans-Neptunian object (229762) 2007 UK126. *A&A*, 600, A12, 16 pp.

Sicardy, B., Ortiz, J. L., Assafin, M., Jehin, E., Maury, A., Lellouch, E. et al. 2011. A Pluto-like radius and a high albedo for the dwarf planet Eris from an occultation. *Nature* 478, 493-496.

Sierks, H., Barbieri, C., Lamy, P. L., Rodrigo, R., Koschny, D., Rickman, H. et al. 2015. On the nucleus structure and activity of comet 67P/Churyumov-Gerasimenko. *Science* 347, aaa1044.

Spencer, J. R., & Moore, J. M. 1992. The influence of thermal inertia on temperatures and frost stability on Triton. *Icarus* 99, 261-272.

Stansberry, J. A., Cruikshank, D. P., Grundy, W. M., Emery, J. P., Osip, D. J., Fernandez, Y. R. et al. 2004. Far-IR Photometry of Centaurs and Kuiper Belt Objects with Spitzer. DPS meeting #36, id.43.01; *BAAS*, Vol. 36, p.1173.

Stansberry, J. A., Grundy, W. M., Margot, J. L., Cruikshank, D. P., Emery, J. P., Rieke, G. H. et al. 2006. The Albedo, Size, and Density of Binary Kuiper Belt Object (47171) 1999 TC36. *ApJ* 643, 556-566.

Stansberry, J., Grundy, W., Brown, M., Cruikshank, D., Spencer, J., Trilling, D., Margot, J.-L. 2008. Physical Properties of Kuiper Belt and Centaur Objects: Constraints from the Spitzer Space Telescope, in *The solar system beyond Neptune*, ed. M. A. Barucci, H. Boehnhardt, D. Cruikshank, A. Morbidelli, Univ. of Arizona Press, Tucson, 161-179.

Stansberry, J. A., Grundy, W. M., Mueller, M., Benecchi, S. D., Rieke, G. H., Noll, K. S. et al. 2012. Physical properties of trans-neptunian binaries (120347) Salacia-Actaea and (42355) Typhon-Echidna. *Icarus* 219, 676-688.

- Stern, S. A., Weintraub, D. A., Festou, M. C. 1993. Evidence for a Low Surface Temperature on Pluto from Millimeter-Wave Thermal Emission Measurements. *Science* 261, 1713-1716.
- Stern, S. A., Grundy, W. M., McKinnon, W. B., Weaver, H. A., Young, L., A. 2018. The Pluto System After New Horizons. *ARA&A* 56, 357-392.
- Sykes, M. V., Cutri, R. M., Lebofsky, L. A., Binzel, R. 1987. IRAS serendipitous survey observations of Pluto and Charon. *Science* 237, 1336-1340.
- Sykes, M. V. & Walker, R. G. 1991. Constraints on the diameter and albedo of 2060 Chiron. *Science* 251, 777-780.
- Sykes, M. V. 1999. IRAS Survey-Mode Observations of Pluto-Charon. *Icarus* 142, 155-159.
- Tedesco, E. F., Veeder, G. J., Dunbar, R. S., Lebofsky, L. A. 1987. IRAS constraints on the sizes of Pluto and Charon. *Nature* 327, 127-129.
- Tegler, S.C., & Romanishin, W. 2000. Extremely red Kuiper-belt objects in near-circular orbits beyond 40 AU. *Nature* 407, 979-981.
- Tegler, S. C., Romanishin, W., & Consolmagno, G. 2016. Two Color Populations of Kuiper Belt and Centaur Objects and the Smaller Orbital Inclinations of Red Centaur Objects. *AJ* 152, 210, 13 pp.
- Thébaud, P. & Doressoudiram, A. 2003. Colors and collision rates within the Kuiper belt: problems with the collisional resurfacing scenario. *Icarus* 162, 27-37.
- Thomas, N., Eggers, S., Ip, W.-H., Lichtenberg, G., Fitzsimmons, A., Jorda, L. et al. 2000. Observations of the Trans-Neptunian Objects 1993 SC and 1996 TL66 with the Infrared Space Observatory. *ApJ* 534, 446-455.
- Verbiscer, A., Porter, S. B., Benecchi, S., Kavelaars, J. J., Weaver, H. A., Spencer, J. R. et al. 2018. Photometric properties of distant KBOs observed by New Horizons LORRI at moderate and high phase angles. The Transneptunian Solar System, March 26-29, 2018, Coimbra, Portugal.
- Vilenius, E., Kiss, C., Mommert, M., Müller, T., Santos-Sanz, P., Pál, A. et al. 2012. TNOs are cool: A survey of the trans-Neptunian region. VI. Herschel/PACS observations and thermal modelling of 19 classical Kuiper Belt objects. *A&A* 541, A94, 17 pp.
- Vilenius, E., Kiss, C., Müller, T., Mommert, M., Santos-Sanz, P., Pál, A. et al. 2014. "TNOs are Cool": A survey of the trans-Neptunian region. X. Analysis of classical Kuiper belt objects from Herschel and Spitzer observations. *A&A* 564, A35, 18 pp.
- Vilenius, E., Stansberry, J., Müller, T., Mueller, M., Kiss, C., Santos-Sanz, P. et al. 2018. "TNOs are Cool": A survey of the trans-Neptunian region. XIV. Size/albedo characterization of the Haumea family observed with Herschel and Spitzer. *A&A* in press, 15 pp.
- Volk, K. & Malhotra, R. 2008. The Scattered Disk as the Source of the Jupiter Family Comets. *ApJ* 687, 714-725.
- Young, L.A. 2013. Pluto's Seasons: New Predictions for New Horizons. *ApJL* 766, L22, 6 pp.
- Wolters, S. D. & Green, S. F. 2009. Investigation of systematic bias in radiometric diameter determination of near-Earth asteroids: the night emission simulated thermal model (NESTM). *MNRAS* 400, 204-218.
- Wong, I. & Brown, M. E. 2016. A Hypothesis for the Color Bimodality of Jupiter Trojans. *AJ* 152, 90, 8 pp.